Physics of Plasmas

RESEARCH ARTICLE | JUNE 12 2024

Localized phase contrast imaging at the Wendelstein 7-X stellarator

S. K. Hansen ; M. Porkolab ; J.-P. Bähner ; A. von Stechow ; O. Grulke ; E. M. Edlund ; the Wendelstein 7-X Team

Phys. Plasmas 31, 062302 (2024)
https://doi.org/10.1063/5.0197958

Physics of Plasmas ARTICLE pubs.aip.org/aip/pop

Localized phase contrast imaging at the Wendelstein 7-X stellarator

Cite as: Phys. Plasmas 31, 062302 (2024); doi: 10.1063/5.0197958
Submitted: 15 January 2024 · Accepted: 27 May 2024 ·
Published Online: 12 June 2024

View Online Export Citation CrossMark

S. K. Hansen,[1,a)] M. Porkolab,[1] J.-P. Bähner,[1] A. von Stechow,[2] O. Grulke,[2,3] E. M. Edlund,[4] and the Wendelstein 7-X Team[b)]

AFFILIATIONS

[1]Plasma Science and Fusion Center, Massachusetts Institute of Technology, Cambridge, Massachusetts 02139, USA
[2]Max-Planck-Institut für Plasmaphysik, D-17491 Greifswald, Germany
[3]Department of Physics, Technical University of Denmark, DK-2800 Kgs. Lyngby, Denmark
[4]State University of New York College at Cortland, Cortland, New York 13045, USA

[a)]Author to whom correspondence should be addressed: soerenkh@psfc.mit.edu
[b)]See the author list in Ref. 2.

ABSTRACT

In its basic form, phase contrast imaging (PCI) provides line-integrated measurements of electron density fluctuations in plasmas. As turbulent fluctuations in magnetically confined plasmas have wave vectors almost perpendicular to the background magnetic field, the signals scattered by fluctuations from different parts of the PCI line-of-sight (LoS) are spatially separated in focal planes of the plasma. This allows localized PCI measurements by placing a mask in such a plane, to only permit signals from specific parts of the LoS to reach the PCI detectors. The present paper describes modeling and design of localization masks for the PCI system at the Wendelstein 7-X (W7-X) stellarator as well as the first results obtained using the masks in the recent long-pulse W7-X experimental campaign. During this project, we have extended the theory describing the mask response within the Fraunhofer diffraction model. As a novel development, we show from first principles that the mask response is determined by the fraction of power of the scattered beam spots that passes the mask. These insights have been used to select the W7-X mask design, consisting of a circular cutout, allowing the unscattered beam spot to pass the mask, with wedges covering a fixed angular range outside the central cutout. In the recent W7-X experimental campaign, the masks have verified the location of the main turbulence features observed by the PCI system and provided new information about the location of short-wavelength magnetohydrodynamic modes.

I. INTRODUCTION

As the largest neoclassically optimized stellarator currently in operation, Wendelstein 7-X (W7-X) plays a key role in advancing the understanding of stellarator turbulence, which effectively determines energy and particle transport in most W7-X plasma scenarios.[1,2] The phase contrast imaging (PCI) system is a major core turbulence diagnostic at W7-X,[3,4] resolving the fluctuating electron density, $\tilde{n}_e$, using the laser phase contrast method.[5] Specifically, PCI provides line-integrated measurements of $\tilde{n}_e$ along the line-of-sight (LoS) of a laser beam intersecting the plasma center.[3,4,6,7] Two linear 32-element detectors observe the line-integrated $\tilde{n}_e$ along a quasi-poloidal direction.[3,4,6,7] This complements other core $\tilde{n}_e$ diagnostics at W7-X, such as Doppler reflectometry[8] and the planned heavy ion beam probe (HIBP).[9] Doppler reflectometry provides localized measurements of the relative density fluctuations at specific wave vectors, $\mathbf{k}$, and positions, determined by the directions and frequencies of the injected microwave beams as well as the plasma profile and magnetic configuration.[8] The HIBP will also provide localized measurements of $\tilde{n}_e$ at three positions simultaneously, depending on the beam acceleration voltage, electrostatic steering plate settings, and magnetic field configuration.[9] Doppler reflectometry and the HIBP further cannot measure turbulence in high density plasma regions, due to the fixed cutoff density at a fixed frequency and magnetic field strength for the former[8] and a low signal-to-noise ratio for the latter.[9] By contrast, PCI is capable of measuring the line-integrated $\tilde{n}_e$ virtually independent of the magnetic field configuration and background plasma parameters. The larger number of detector elements additionally means that PCI measurements cover a larger region of $\mathbf{k}$ space than Doppler reflectometry

or the HIBP. Thus, PCI is capable of characterizing magnetic configuration effects on turbulence for a large range of plasma parameters[10] as well as measuring Alfvén eigenmodes.[3,4,11,12] To enhance PCI capabilities at W7-X, the ability to locate the region of origin of the signal is, however, highly desirable.

The radial distribution of $\tilde{n}_e$ can be inferred indirectly from PCI. This may be done by combining experiments with reversed equilibrium magnetic fields and theoretical modeling,[6] reproduction of measured signals using synthetic PCI techniques,[6,7,13–15] and mapping the measured signal along specific directions to specific plasma regions.[5,15–20] The regions from which the various PCI signal features at W7-X originate have previously been explored in electron cyclotron resonance heated (ECRH) plasmas.[6,7] Such investigations indicate that the majority of the PCI signal originates from the region around the maximum of the rotational speed due to the neoclassical radial electric field, E_r,[6] and that the rotation direction is linked to the signal from the inboard or outboard side.[6,7] In nonstandard scenarios, e.g., during improved performance after pellet injection,[1,2] localization by this method is ambiguous, as multiple characteristic phase velocities are observed.[21] To improve the understanding of turbulence in such scenarios, it is necessary to augment the W7-X PCI system with the ability to localize $\tilde{n}_e$ based on less scenario-specific methods.

Two general methods of localizing a PCI signal have been established previously. The first method uses a two-dimensional detector array to extract the direction of the fluctuations through data analysis techniques, which can then be mapped to specific parts of the LoS.[17,19] At LHD,[17,19] localization down to approximately 10% of the minor radius is, thus, possible using maximum entropy data analysis methods.[19] A similar effect can be obtained for steady-state plasmas by scanning a one-channel detector in a two-dimensional pattern, which was also demonstrated at LHD.[22] Such a scanning detector has been installed at W7-X and will be compared with the second method in a future publication. The second method involves only permitting parts of the signal with specific fluctuation directions to reach the PCI detectors,[23] by placing a mask in a focal plane of the laser beam.[4,5,15,18,20] This method has been demonstrated at Heliotron E,[5] Alcator C-Mod,[16] DIII-D,[18] and TCV,[15] and some preliminary investigations were carried out in previous W7-X experimental campaigns as well.[4] Earlier studies mainly utilized simple mask designs with a straight slit of constant width.[4,5,15,16,18] Such masks provide good localization while allowing a significant fraction of the PCI signal to pass, but complicate the interpretation of the data.[4,18] In this paper, we, therefore, investigate the performance of alternative mask designs numerically and analytically using synthetic PCI techniques[7,15] to obtain mask results that can be interpreted in a straightforward manner. These mask designs have been manufactured and tested during the first long-pulse W7-X experimental campaign.[24] We report the mask results and compare them with theoretical expectations from synthetic PCI[7] as well as a novel simplified model.

The paper is organized as follows: Sec. II describes the theory of PCI localization masks, including the newly developed simplified mask model. Section III presents the numerical and analytical investigations used for the W7-X mask design. Section IV shows comparisons of PCI mask measurements from the first long-pulse W7-X experimental campaign[24] with the simplified model. Finally, Sec. V presents our conclusions and an outlook.

II. THEORY

A detailed theoretical description of the operating principle of the W7-X PCI diagnostic is given in Ref. 7. We, therefore, focus on the details required for modeling the system including a mask and refer to Ref. 7 for further details. A schematic of the W7-X PCI system with a mask is seen in Fig. 1. The PCI system is described using the Fraunhofer diffraction model of Refs. 7, 15, and 25. In this framework, the electric field of the PCI laser beam after passing the plasma and an

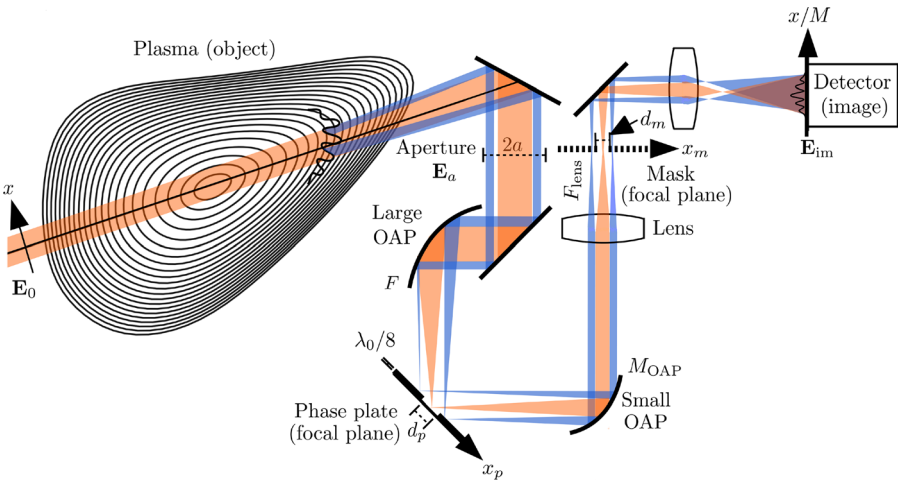

FIG. 1. Schematic of the essential components of the W7-X PCI system when operating with a localization mask. Trajectories of the unscattered and scattered signal components are marked by the orange and blue beams, respectively. A laser beam, with electric field profile $\mathbf{E}_0$ and vacuum wavelength λ_0, passes through the W7-X plasma from the inboard to the outboard side and is cut by a circular aperture of radius a, yielding an electric field $\mathbf{E}_a$. Next, the beam is focused onto a phase plate, possessing a groove width d_p, by a large OAP with focal length F. After passing the phase plate, the beam reaches a small OAP, which forms telescope of magnification M_{OAP} with the large OAP. The magnified beam is then focused onto the mask, possessing a central opening of d_m, by a lens with focal length F_{lens}. Finally, the beam is imaged onto the detector array by additional optical elements. The net magnification of the optical system is M.

aperture (defined by the port liner with radius $a = 42$ mm at W7-X,[7] cf. Fig. 1) is

$$\mathbf{E}_a = \mathcal{P}_a \mathbf{E}_0 \, e^{i\phi}. \quad (1)$$

Here, $\mathcal{P}_a$ is the pupil function of the aperture, with a value of one inside the opening and zero outside the opening, $\mathbf{E}_0$ is the laser beam electric field profile, and ϕ ($\propto$ the line-integrated $\tilde{n}_e$ along the LoS[7]) is the phase shift introduced by passing through the plasma. Next, the laser beam is focused onto the phase plate and mask, seen in Fig. 1. In the phase plate and mask focal planes, the electric field profile is proportional to the Fourier transform of $\mathbf{E}_a$, defined as $\mathcal{F}(\mathbf{E}_a) = \int_{\text{all } \mathbf{x}_\perp} \mathbf{E}_a \, e^{-i\mathbf{k}'\cdot\mathbf{x}_\perp} \, d\mathbf{x}_\perp$, where $\mathbf{x}_\perp$ is the position coordinate perpendicular to the beam axis in the plasma and $\mathbf{k}'$ is the wave vector of the Fourier mode. The phase plate and mask introduce transfer functions, T_p and $\mathcal{P}_m$, respectively, such that the profile after passing the last element is $\propto T_p \mathcal{P}_m \mathcal{F}(\mathbf{E}_a)$. As suggested by the notation, $\mathcal{P}_m$ is the pupil function of the mask. The phase plate is an essential component of any PCI system, shifting the phase of small-k' components hitting a central groove on the phase plate by $\pm\pi/2$ relative to large-k' components outside the groove. This effectively converts the phase shift due to $\tilde{n}_e$ in Eq. (1) into an amplitude modulation, which can be imaged by standard infrared detectors, as demonstrated in Subsection II A and Ref. 7. The transfer function of the grooved mirror phase plate at W7-X (cf. Fig. 1) is $T_p = i\sqrt{\rho}\mathcal{P}_{\mathbf{k}'\in\text{groove}} + \mathcal{P}_{\mathbf{k}'\notin\text{groove}}$, with $\rho = 0.28$ being the fraction of beam power reflected by the phase plate groove.[3,4,7] All mask-related results also hold when $T_p = -i\sqrt{\rho}\mathcal{P}_{\mathbf{k}'\in\text{groove}} + \mathcal{P}_{\mathbf{k}'\notin\text{groove}}$, which we indicate by setting $T_p = \pm i\sqrt{\rho}\mathcal{P}_{\mathbf{k}'\in\text{groove}} + \mathcal{P}_{\mathbf{k}'\notin\text{groove}}$ in the following. Finally, the beam is imaged onto detectors placed at an image plane of the plasma, as seen in Fig. 1. In the image plane, the electric field profile is proportional to the inverse Fourier transform of $T_p\mathcal{P}_m\mathcal{F}(\mathbf{E}_a)$, defined as $\mathcal{F}^{-1}[T_p\mathcal{P}_m\mathcal{F}(\mathbf{E}_a)] = [1/(2\pi)^2]\int_{\text{all}\mathbf{k}'} T_p\mathcal{P}_m\mathcal{F}(\mathbf{E}_a) e^{i\mathbf{k}'\cdot\mathbf{x}_\perp} d\mathbf{k}'$. Following Ref. 7, the variable net magnification of the PCI system, M, given by the ratio of distances in the plasma to distances in the detector image plane (cf. Fig. 1 and Refs. 4 and 7) is used to scale distances in the image plane to be equal to those in the plasma. The electric field profile in the scaled image plane is

$$\mathbf{E}_{\text{im}} = e^{i\phi_{\text{im}}} \mathcal{F}^{-1}\left[T_p \mathcal{P}_m \mathcal{F}(\mathbf{E}_a)\right], \quad (2)$$

with ϕ_{im} being the phase shift in the PCI system after the plasma. The full PCI signal is computed by integrating the beam intensity, $I_{\text{im}} = |\mathbf{E}_{\text{im}}|^2/(2\eta_0) = |\mathcal{F}^{-1}[T_p\mathcal{P}_m\mathcal{F}(\mathbf{E}_a)]|^2/(2\eta_0)$, where η_0 is the impedance of vacuum, over the PCI detector elements scaled by M, while applying the detector response functions, as described in Ref. 7.

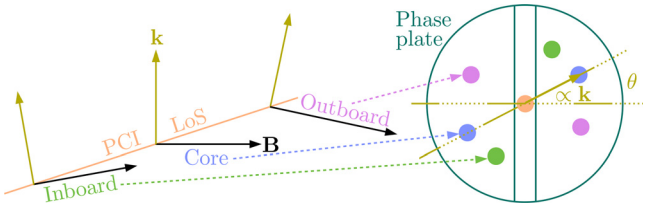

FIG. 2. $\tilde{n}_e$ in magnetically confined plasmas have **k** almost perpendicular to **B**. Furthermore, the **k** observed by a PCI system is perpendicular to the laser LoS, making its direction a function of the pitch angle of **B**, as illustrated on the left. Signals due to fluctuations at different parts of the LoS are, thus, spatially separated in focal planes of the plasma, as illustrated on the right. Localization is obtained by placing a mask in such a plane cutting off the signal outside the region of interest.

A. Simplified model

Although Eq. (2) describes the PCI response when a mask is placed in a focal plane within the theoretical framework of Refs. 7, 15, and 25 it does not immediately reveal the localization properties. We, therefore, develop a simplified model based on a few generally valid assumptions. We first assume that $\phi = \phi_0 + \tilde{\phi}$, where ϕ_0 is a background phase shift, varying slowly across the laser beam, and $\tilde{\phi}$ is a fluctuating phase shift, satisfying $|\tilde{\phi}| \ll 1$. With these assumptions, $e^{i\phi} \approx e^{i\phi_0}(1 + i\tilde{\phi})$ and $e^{i\phi_0}$ can be considered constant across the laser beam.[25] We further consider the response to a real Fourier mode, $\tilde{\phi} = A\, e^{i\mathbf{k}\cdot\mathbf{x}_\perp} + A^* e^{-i\mathbf{k}\cdot\mathbf{x}_\perp}$, where $\mathbf{k}$ is the fluctuation wave vector and A is the mode amplitude, satisfying $|A| \ll 1$. Inserting the above expressions in Eq. (1) and performing a Fourier transform then yields

$$\mathcal{F}(\mathbf{E}_a) \approx e^{i\phi_0}\left[\mathcal{F}(\mathcal{P}_a\mathbf{E}_0) + iA\mathcal{F}(\mathcal{P}_a\mathbf{E}_0)(\mathbf{k}'-\mathbf{k}) + iA^*\mathcal{F}(\mathcal{P}_a\mathbf{E}_0)(\mathbf{k}'+\mathbf{k})\right], \quad (3)$$

where $\mathcal{F}(\mathcal{P}_a\mathbf{E}_0)(\mathbf{k}' \pm \mathbf{k})$ denote $\mathcal{F}(\mathcal{P}_a\mathbf{E}_0)$ with $\mathbf{k}'$ replaced by $\mathbf{k}' \pm \mathbf{k}$, respectively. Equation (3) shows that the initial beam pattern in the focal plane can be approximated by the Fourier transform of the laser beam pattern truncated by the aperture, $\mathcal{F}(\mathcal{P}_a\mathbf{E}_0)$, and the same pattern centered around $\mathbf{k}$, $iA\mathcal{F}(\mathcal{P}_a\mathbf{E}_0)(\mathbf{k}' - \mathbf{k})$, and $-\mathbf{k}$, $iA^*\mathcal{F}(\mathcal{P}_a\mathbf{E}_0)(\mathbf{k}' + \mathbf{k})$; the latter two beam spots are scattered by the fluctuation (cf. Figs. 1–3). We next compute $T_p\mathcal{P}_m\mathcal{F}(\mathbf{E}_a)$, assuming that the unscattered beam spot is fully contained in the phase plate groove and that the scattered beam spots are fully outside the phase plate groove. With this assumption

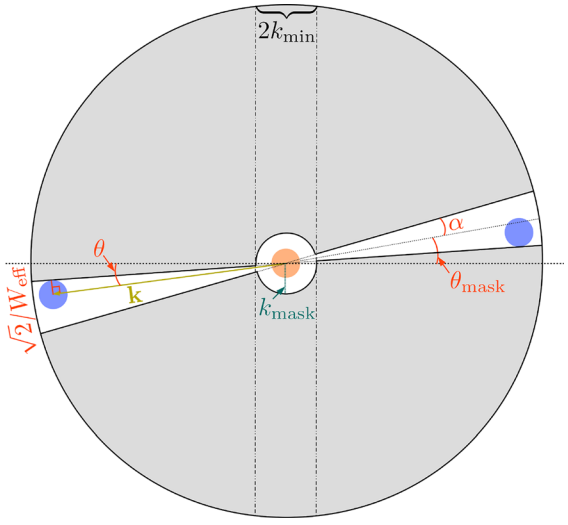

FIG. 3. Illustration of the mask and phase plate used at W7-X in $\mathbf{k}'$ space. The central mask cutout covers $k' < k_{\text{mask}}$, while the phase plate slit covers $|k'_x| < k_{\text{min}}$; for the W7-X mask design $k_{\text{mask}} = k_{\text{min}}$. Outside the central cutout, the mask has two wedge openings with constant half-opening angles α. The angle between the mask symmetry axis and the k'_x axis is θ_{mask}. Unscattered and scattered beam spots (orange and blue circles, respectively) are separated by a fluctuation wave vector **k**, forming an angle θ with the k'_x axis. Using an effective Gaussian beam model, the 1/e intensity beam spot radius in $\mathbf{k}'$ space is $\sqrt{2}/W_{\text{eff}}$.

$$T_p\mathcal{P}_m\mathcal{F}(\mathbf{E}_a) \approx \mathrm{i}\,\mathrm{e}^{\mathrm{i}\phi_0}\mathcal{P}_m[\pm\sqrt{\rho}\mathcal{F}(\mathcal{P}_a\mathbf{E}_0) + A\mathcal{F}(\mathcal{P}_a\mathbf{E}_0)(\mathbf{k}'-\mathbf{k}) + A^*\mathcal{F}(\mathcal{P}_a\mathbf{E}_0)(\mathbf{k}'+\mathbf{k})]. \tag{4}$$

Plugging Eq. (4) into Eq. (2), we finally find

$$\mathbf{E}_{\mathrm{im}} \approx \mathrm{i}\,\mathrm{e}^{\mathrm{i}(\phi_0+\phi_{\mathrm{im}})}\{\pm\sqrt{\rho}\mathcal{F}^{-1}[\mathcal{P}_m\mathcal{F}(\mathcal{P}_a\mathbf{E}_0)] + A\mathcal{F}^{-1}\left[\mathcal{P}_m\mathcal{F}(\mathcal{P}_a\mathbf{E}_0)(\mathbf{k}'-\mathbf{k})\right] + A^*\mathcal{F}^{-1}\left[\mathcal{P}_m\mathcal{F}(\mathcal{P}_a\mathbf{E}_0)(\mathbf{k}'+\mathbf{k})\right]\}. \tag{5}$$

To obtain a mask response function, we note that without a mask ($\mathcal{P}_m = 1$), $\mathbf{E}_{\mathrm{im}} \approx \mathrm{i}\,\mathrm{e}^{\mathrm{i}(\phi_0+\phi_{\mathrm{im}})}\mathcal{P}_a\mathbf{E}_0\left(\pm\sqrt{\rho} + A\,\mathrm{e}^{\mathrm{i}\mathbf{k}\cdot\mathbf{x}_\perp} + A^*\,\mathrm{e}^{-\mathrm{i}\mathbf{k}\cdot\mathbf{x}_\perp}\right)$. We, therefore, fit Eq. (5) using a function of this form with different weights for the unscattered (m_0) and scattered ($m_{\mathbf{k}}$) beam spots,

$$\mathbf{E}_{\mathrm{fit}} = \mathrm{i}\,\mathrm{e}^{\mathrm{i}(\phi_0+\phi_{\mathrm{im}})}\mathcal{P}_a\mathbf{E}_0\left[\pm m_0\sqrt{\rho} + m_{\mathbf{k}}(A\,\mathrm{e}^{\mathrm{i}\mathbf{k}\cdot\mathbf{x}_\perp} + A^*\,\mathrm{e}^{-\mathrm{i}\mathbf{k}\cdot\mathbf{x}_\perp})\right]. \tag{6}$$

As shown in Appendix A, the least squares fit of Eq. (5) to Eq. (6) gives

$$m_0 = \frac{\int_{\text{all }\mathbf{k}'\notin\text{mask}} |\mathcal{F}(\mathcal{P}_a\mathbf{E}_0)|^2\,\mathrm{d}\mathbf{k}'}{\int_{\text{all }\mathbf{k}'} |\mathcal{F}(\mathcal{P}_a\mathbf{E}_0)|^2\,\mathrm{d}\mathbf{k}'}, \tag{7}$$

$$m_{\mathbf{k}} = \frac{\int_{\text{all }\mathbf{k}'\notin\text{mask}} \left[|\mathcal{F}(\mathcal{P}_a\mathbf{E}_0)(\mathbf{k}'-\mathbf{k})|^2 + |\mathcal{F}(\mathcal{P}_a\mathbf{E}_0)(\mathbf{k}'+\mathbf{k})|^2\right]\mathrm{d}\mathbf{k}'}{\int_{\text{all }\mathbf{k}'} \left[|\mathcal{F}(\mathcal{P}_a\mathbf{E}_0)(\mathbf{k}'-\mathbf{k})|^2 + |\mathcal{F}(\mathcal{P}_a\mathbf{E}_0)(\mathbf{k}'+\mathbf{k})|^2\right]\mathrm{d}\mathbf{k}'}. \tag{8}$$

From Eqs. (7) and (8), m_0 and $m_{\mathbf{k}}$ are the fractions of power of the unscattered and scattered beam spots transmitted by the mask, respectively. Inserting this in Eq. (6), the simplified mask model amounts to multiplying the amplitude of the unscattered/scattered signal component by the fraction of power in the corresponding beam spots transmitted by the mask, proving the statements in Subsection IV A of Ref. 18. To model the effect of the mask on the PCI signal, we compute

$$I_{\mathrm{fit}} = \frac{|\mathbf{E}_{\mathrm{fit}}|^2}{2\eta_0} \approx \frac{|\mathcal{P}_a\mathbf{E}_0|^2}{2\eta_0}\left[m_0^2\rho \pm m_{\mathbf{k}}m_0 2\sqrt{\rho}(A\,\mathrm{e}^{\mathrm{i}\mathbf{k}\cdot\mathbf{x}_\perp} + A^*\,\mathrm{e}^{-\mathrm{i}\mathbf{k}\cdot\mathbf{x}_\perp})\right]. \tag{9}$$

Equation (9) shows that the simplified model is equivalent to employing a model without a mask, such as the one in Refs. 6 and 7, if the DC detector power is multiplied by $\mathcal{M}_0 = m_0^2$, and the AC detector power of wave mode $\mathbf{k}$ is multiplied by $\mathcal{M}_{\mathbf{k}} = m_{\mathbf{k}}m_0$. The localization properties are, thus, determined by $m_{\mathbf{k}}$, while m_0 determines the noise level.[7] Equation (9) implies that the signal-to-noise ratio is $\propto 1/m_0$ (based on Ref. 3) and that it is, therefore, beneficial to cut off a significant fraction of the unscattered beam spot power using the mask. We do, however, note that this will also cause increased diffraction of the beam spot, reducing the ability of Eq. (9) to describe the actual PCI signal.

B. Localized phase contrast imaging in magnetically confined plasmas

To apply the above models to the problem of obtaining localized PCI measurements in magnetically confined plasmas, regardless of geometry, we assume that the turbulent plasma fluctuations have $\mathbf{k}$ almost perpendicular to the background magnetic field, $\mathbf{B}$.[18] As the $\mathbf{k}$ observed by PCI is further perpendicular to the laser LoS, this makes the angle of the observed $\mathbf{k}$, θ, a function of the pitch angle of $\mathbf{B}$. Since the pitch angle of $\mathbf{B}$ varies across the PCI LoS, each θ can be mapped to a specific region in the plasma, as illustrated in Fig. 2. Thus, by installing a mask in a focal plane that only permits scattered beam spots in a specific θ range to pass, PCI measurements can be localized.

The variation of θ across the central PCI LoS in different W7-X magnetic field configurations is shown in Fig. 6 of Ref. 4. It is monotonic, but relatively small for all configurations, being close to 5° on the inboard side and ranging from 14° to 18° on the outboard side.[4] Localization is, thus, mainly possible on the outboard side of W7-X, as shown in Sec. III.

III. DESIGN AND MODELING OF LOCALIZATION MASKS FOR W7-X

Before turning to the specific design used for localization masks at W7-X, we determine the physical dimensions of a mask corresponding to specific $\mathbf{k}$ values in the mask focal plane. A schematic of the mask location in the W7-X PCI system is shown in Fig. 1. The mask is located in a different focal plane than the phase plate. To determine the dimensions of the mask corresponding to a particular $\mathbf{k}$ value, we note that $\mathbf{k}$ can be mapped to positions on the phase plate, $\mathbf{x}_{\perp p}$, as follows:[4,18]

$$\mathbf{x}_{\perp p} = \frac{\lambda_0 F}{2\pi}\mathbf{k}. \tag{10}$$

Here, the origin of $\mathbf{x}_{\perp p}$ is the center of the unscattered beam spot (cf. Fig. 1), $\lambda_0 = 10.6\,\mu$m is the vacuum wavelength of the PCI laser beam, and $F = 80'' = 2.032$ m is the focal length of the large off-axis parabolic (OAP) mirror in front of the phase plate.[7,18] Using Eq. (10), the smallest k at the edge of the phase plate groove, k_{min}, is

$$k_{\mathrm{min}} = \frac{\pi d_p}{\lambda_0 F}, \tag{11}$$

where d_p is the width of the phase plate groove. At W7-X, $d_p = 1.1$ mm,[4] giving $k_{\mathrm{min}} = 1.6\,\mathrm{cm}^{-1}$. As seen in Fig. 1, a small OAP mirror is placed after the phase plate. The small OAP mirror forms a telescope with the large OAP mirror, resulting in a collimated laser beam magnified by $M_{\mathrm{OAP}} = 0.075$ relative to the beam size in the plasma after the small OAP mirror.[4] Next, the magnified collimated beam is focused onto the mask by a lens with focal length, $F_{\mathrm{lens}} = 16'' = 0.4064$ m. The wave vector corresponding to $\mathbf{k}$ in the magnified beam is $\mathbf{k}/M_{\mathrm{OAP}}$, and in the thin-lens approximation,[26] the effect of the lens is equivalent to that of the focusing mirror with $F \to F_{\mathrm{lens}}$. Thus, the position corresponding to $\mathbf{k}$ in the mask plane, $\mathbf{x}_{\perp m}$, becomes

$$\mathbf{x}_{\perp m} = \frac{\lambda_0 F_{\mathrm{lens}}}{2\pi M_{\mathrm{OAP}}}\mathbf{k}, \tag{12}$$

with the origin of $\mathbf{x}_{\perp m}$ being the center of the unscattered beam spot (cf. Fig. 1). The $\mathbf{k}$ corresponding to the dimensions of a central cutout required to allow the unscattered beam spot to pass through the mask, k_{mask}, is calculated similarly to Eq. (11),

$$k_{\mathrm{mask}} = \frac{\pi M_{\mathrm{OAP}} d_m}{\lambda_0 F_{\mathrm{lens}}}, \tag{13}$$

where d_m is the diameter of a circular central mask cutout, or the width of a straight mask groove (cf. Fig. 1). Taking the ratio of Eqs. (11) and (13) allows d_m to be expressed by d_p,

$$d_m = \frac{k_{\mathrm{mask}}}{k_{\mathrm{min}}}\frac{F_{\mathrm{lens}}}{F}\frac{d_p}{M_{\mathrm{OAP}}}. \tag{14}$$

Setting $k_{\mathrm{min}} = k_{\mathrm{mask}}$, a value of $d_m = 2.9$ mm is obtained at W7-X.

A number of localization mask designs were considered for W7-X. In all cases, the mask properties could be understood based on the response from Eqs. (7) and (8), combined with the $m_{\mathbf{k}}$ model of Appendix B. Two criteria were considered to be of primary importance for the final mask design. First, the mask should allow the unscattered beam spot to pass without significant clipping to minimize its effect on the DC beam pattern, i.e., have $m_0 \approx 1$. As seen in Fig. 3, this is addressed by a central circular cutout with $k_{\mathrm{mask}} = k_{\mathrm{min}} = 1.6\,\mathrm{cm}^{-1}$ ($d_m = 2.9$ mm), which is chosen since there is no phase contrast for fluctuations with $k < k_{\mathrm{min}}$. Second, the mask response should correspond as closely as possible to a fixed region in the plasma to simplify the interpretation of the results. As illustrated in Fig. 2, this can be achieved by mask openings covering a fixed θ range. The chosen mask design, seen in Fig. 3, incorporates this by two wedge openings, separated by an angle of π, each with a constant half-opening angle of $\alpha < \pi/2$ outside the central circular cutout. These openings enable the beam spots scattered by $\pm\mathbf{k}$ to pass through the mask whenever one of them is inside the mask opening if the unscattered beam spot is centered on the mask (cf. Fig. 3). The remainder of this section is dedicated to calculating m_0 and $m_{\mathbf{k}}$ for Gaussian beams with the W7-X mask design in Fig. 3; the corresponding results for the commonly employed straight mask design[5,15,16,18] are found in Appendix C. We further determine the limits of localization with a mask due to the finite focal plane beam spot size and compare the simplified mask model with results based on Eq. (2).

A. Mask response for the unscattered beam spot

As a first step, we demonstrate that $m_0 \approx 1$ for the chosen k_{mask} and typical PCI laser beam parameters at W7-X, i.e., that the first mask design criterion is fulfilled. We set

$$\mathbf{E}_0 = \mathbf{E}_0(0)\,\mathrm{e}^{-r^2/W^2}, \tag{15}$$

where r is the distance from the beam axis and W is the 1/e electric field beam radius. Combining Eq. (15) and $\mathcal{P}_a = \Theta(a - r)$, where Θ is the Heaviside function and $a = 42$ mm is the radius of the W7-X port liner aperture[7] (cf. Fig. 1), then yields

$$\mathcal{F}(\mathcal{P}_a\mathbf{E}_0) = 2\pi\mathbf{E}_0(0)\int_0^a r\,J_0(k'r)\,\mathrm{e}^{-r^2/W^2}\,\mathrm{d}r, \tag{16}$$

with J_0 being the Bessel function of the first kind of order zero.[27] Next, we note that the denominator of Eq. (7) can be evaluated using Parseval's theorem and performing the resulting integral in polar coordinates,

$$\int_{\mathrm{all}\,\mathbf{k}'}|\mathcal{F}(\mathcal{P}_a\mathbf{E}_0)|^2\,\mathrm{d}\mathbf{k}' = (2\pi)^2\int_{\mathrm{all}\,\mathbf{r}}|\mathcal{P}_a\mathbf{E}_0|^2\,\mathrm{d}\mathbf{r} = 2\pi^3(1-\mathrm{e}^{-2a^2/W^2})W^2|\mathbf{E}_0(0)|^2. \tag{17}$$

The numerator of Eq. (7) is evaluated by performing the $\mathbf{k}'$ integral in polar coordinates over $k' \in]0,\infty[$ for the θ' range of 4α covered by the wedges and over $k' \in]0, k_{\mathrm{mask}}[$ for the remaining θ' range of $2\pi - 4\alpha$ (cf. Fig. 3), exploiting the θ' symmetry of Eq. (16). When combined, the above results yield

$$m_0 = \left(1-\frac{2\alpha}{\pi}\right)\frac{4}{(1-\mathrm{e}^{-2a^2/W^2})W^2} \times \int_0^{k_{\mathrm{mask}}} k'\left[\int_0^a r\,J_0(k'r)\,\mathrm{e}^{-r^2/W^2}\,\mathrm{d}r\right]^2\mathrm{d}k' + \frac{2\alpha}{\pi}. \tag{18}$$

In general, Eq. (18) cannot be evaluated analytically. It does, however, involve integration of a well-behaved integrand over a finite domain, making it suitable for numerical evaluation, which is performed using normalized integration variables ($\zeta = k'W$, $\xi = r/W$),

$$m_0 = \left(1-\frac{2\alpha}{\pi}\right)\frac{4}{1-\mathrm{e}^{-2a^2/W^2}}\int_0^{k_{\mathrm{mask}}W}\zeta\left[\int_0^{a/W}\xi J_0(\zeta\xi)\,\mathrm{e}^{-\xi^2}\mathrm{d}\xi\right]^2\mathrm{d}\zeta + \frac{2\alpha}{\pi}. \tag{19}$$

The value of Eq. (19) is computed using the `nquad` function from SciPy. When $a \to \infty$, $\mathrm{e}^{-2a^2/W^2} \to 0$ and the integrals in Eq. (19) can be evaluated analytically,[28] giving

$$m_0(\mathrm{Gaussian}) = 1 - \left(1-\frac{2\alpha}{\pi}\right)\mathrm{e}^{-k_{\mathrm{mask}}^2W^2/2}. \tag{20}$$

This is the result for a Gaussian beam in the absence of an aperture. For $W \to \infty$, we can use $\xi\,\mathrm{e}^{-\xi^2} \approx \xi$ (which again allows the integrals in Eq. (19) to be evaluated analytically[28]) along with $1 - \mathrm{e}^{-2a^2/W^2} \to 2a^2/W^2$, to obtain

$$m_0(\mathrm{Airy\ Disk}) = 1 - \left(1-\frac{2\alpha}{\pi}\right)\left[J_0^2(k_{\mathrm{mask}}a) + J_1^2(k_{\mathrm{mask}}a)\right], \tag{21}$$

where J_1 is the Bessel function of the first kind of order one.[27] Equation (21) is also the m_0 for an Airy disk diffraction pattern, resulting from a uniform plane wave truncated by a circular aperture in the object plane.[29] We plot the exact m_0 from Eq. (19), along with the Gaussian and Airy disk m_0 from Eqs. (20) and (21), vs W/a for $k_{\mathrm{mask}}a = 6.74$ (corresponding to the value at W7-X) and $\alpha = 5°$ in Fig. 4. The exact m_0 follows the Gaussian m_0 closely for small W/a, but eventually reaches a maximum, above which m_0 decreases, approaching the value of the Airy disk diffraction pattern for $W/a \to \infty$. This behavior can be understood by noting that the diffraction pattern due to the circular aperture has broader tails than that of a purely Gaussian beam in the focal plane. Specifically, the intensity of the Airy disk diffraction pattern is $\propto J_1^2(k'a)/(k'a)^2$, while that of a Gaussian beam spot is $\propto \mathrm{e}^{-k^2W^2/2}$. This means that the reduction of the primary beam spot size associated with increasing W, leading to an increase in m_0 with W/a, is at some point offset by the broader tails due to diffraction from the aperture, resulting in an m_0 maximum. The maximum of m_0 occurs near $W = \sqrt{2a/k_{\mathrm{mask}}}$, i.e., the point at which the fraction of power transmitted through the central cutout of the mask matches the fraction of power transmitted through the aperture in the Gaussian approximation. For the W7-X PCI system, $\sqrt{2a/k_{\mathrm{mask}}} = 22.9$ mm, while the numerically determined maximum of m_0 occurs at $W = 23.7$ mm. Although the typical value of $W = 40$ mm at W7-X is above the maximum of m_0, the $\alpha = 5°$ mask, which is the smallest α

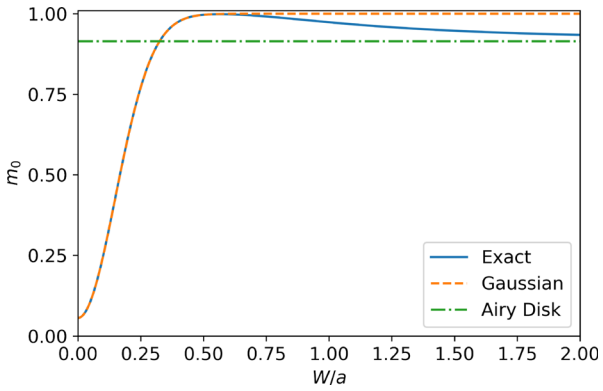

FIG. 4. m_0 vs W/a using the exact (solid line), Gaussian (dashed line), and Airy disk (dashed-dotted line) models for the W7-X mask design with $k_{\text{mask}}a = 6.74$ and $\alpha = 5°$. The exact m_0 is seen to follow the Gaussian one at small W/a, reach a peak at an intermediate $W/a \approx \sqrt{2}/(k_{\text{mask}}a)$, and to approach the Airy disk value when $W/a \to \infty$.

used at W7-X for reasons discussed below, still has $m_0 = 0.977$ in this case. Thus, the masks used at W7-X cut off only a small part of the unscattered beam spot power, indicating that they satisfy the first criterion considered for the design.

B. Mask localization properties

We now turn to the issue of finding $m_{\mathbf{k}}$, which determines the mask localization properties. While it is not feasible to find a general closed form of $m_{\mathbf{k}}$ using Eq. (8) with $\mathcal{F}(\mathcal{P}_a\mathbf{E}_0)$ from Eq. (16), an approximate form, valid for $k > k_{\text{mask}}$, can be obtained analytically. The details of the calculation are given in Appendix B, so here we shall simply quote the result of Eq. (B6) for the mask design used at W7-X,

$$m_{\mathbf{k}} \approx 1 + \frac{1}{4}\operatorname{erfc}\left[\frac{(k_{\text{mask}}-k)W_{\text{eff}}}{\sqrt{2}}\right]\left\{\operatorname{erf}\left[\frac{kW_{\text{eff}}}{\sqrt{2}}(\theta_{\text{mask}}+\alpha-\theta)\right] - \operatorname{erf}\left[\frac{kW_{\text{eff}}}{\sqrt{2}}(\theta_{\text{mask}}-\alpha-\theta)\right] + \operatorname{erf}\left[\frac{kW_{\text{eff}}}{\sqrt{2}}(\theta_{\text{mask}}+\alpha-\theta-\pi)\right] - \operatorname{erf}\left[\frac{kW_{\text{eff}}}{\sqrt{2}}(\theta_{\text{mask}}-\alpha-\theta-\pi)\right] - 2\right\}, \tag{22}$$

while noting that $\theta_{\text{mask}} - \theta$ should be mapped to the region $[-\pi/2, 3\pi/2]$ for the expression to be valid. In Eq. (22), θ_{mask} is the angle between the mask symmetry axis and the k'_x axis (cf. Fig. 3), W_{eff} is an effective Gaussian beam radius taking diffraction from the aperture into account,[20] and erf/erfc are the error/complementary error functions, respectively.[27] We further note that Eq. (B6) allows α to be a function of k determined by the mask design, e.g., $\alpha = \arcsin(k_{\text{mask}}/k)$ (for $k > k_{\text{mask}}$) or $\pi/2$ (for $k < k_{\text{mask}}$) in the straight mask case from Appendix C. For the mask design employed at W7-X, α is, however, constant. As expected from Fig. 2, this indicates that the W7-X masks localize the response to a fixed angular range as closely as possible, which was the second mask design criterion.

We can interpret Eq. (22) by consulting Fig. 3. Equation (22) models the scattered beam spots as Gaussian, with an effective 1/e intensity radius in $\mathbf{k}'$ space given by $\sqrt{2}/W_{\text{eff}}$. The erfc term in Eq. (22) models the transition from the central circular cutout to the wedge region occurring around $k = k_{\text{mask}}$; the k half-width of the transition region, $\sqrt{2}/W_{\text{eff}}$, is given by the beam spot radius, as expected. For $k \ll k_{\text{mask}}$, $\operatorname{erfc}[(k_{\text{mask}}-k)W_{\text{eff}}/\sqrt{2}] \to 0$, such that $m_{\mathbf{k}} \approx 1$, indicating that the mask allows beam spots scattered by a small $\mathbf{k}$ to pass through the central cutout regardless of θ. On the other hand, for $k \gg k_{\text{mask}}$, $\operatorname{erfc}[(k_{\text{mask}}-k)W_{\text{eff}}/\sqrt{2}] \to 2$, resulting in

$$m_{\mathbf{k}} \approx \frac{1}{2}\left\{\operatorname{erf}\left[\frac{kW_{\text{eff}}}{\sqrt{2}}(\theta_{\text{mask}}+\alpha-\theta)\right] - \operatorname{erf}\left[\frac{kW_{\text{eff}}}{\sqrt{2}}(\theta_{\text{mask}}-\alpha-\theta)\right] + \operatorname{erf}\left[\frac{kW_{\text{eff}}}{\sqrt{2}}(\theta_{\text{mask}}+\alpha-\theta-\pi)\right] - \operatorname{erf}\left[\frac{kW_{\text{eff}}}{\sqrt{2}}(\theta_{\text{mask}}-\alpha-\theta-\pi)\right]\right\}. \tag{23}$$

The effect of the wedge openings can be understood from Eq. (23). When $\theta_{\text{mask}} - \theta \in]-\alpha, \alpha[$ or $]\pi-\alpha, \pi+\alpha[$ and $kW_{\text{eff}}/\sqrt{2} \gg 1$, $m_{\mathbf{k}} \approx 1$, while $m_{\mathbf{k}} \approx 0$ for other $\theta_{\text{mask}} - \theta$ values. This indicates that the mask allows the beam spots to pass if the they are inside the angles covered by the mask wedge openings, as expected. The angular half-width of the transition regions around $\theta_{\text{mask}} - \theta = \pm\alpha$ and $\pi \pm \alpha$ is $\sqrt{2}/(kW_{\text{eff}})$, which is the half-angle covered by a beam spot scattered by $\mathbf{k}$, assuming $\sqrt{2}/(kW_{\text{eff}}) \ll 1$, as seen in Fig. 3. This illustrates that it is generally easier to obtain localized measurements for large-k fluctuations, in agreement with previous investigations.[5,18,20] It further indicates that the smallest α allowing a significant fraction of the scattered beam spot power to pass at a given k with a centered unscattered beam spot is $\approx \sqrt{2}/(kW_{\text{eff}})$. To determine this α, we compute the W_{eff} appropriate for Eq. (16). This is done using the method of Ref. 30, which matches the Maclaurin series of $|\mathcal{F}(\mathcal{P}_a\mathbf{E}_0)|^2$ from Eq. (16) to that of the effective Gaussian fit, $|\hat{\mathbf{E}}_{\text{fit}}(0)|^2 e^{-k^2W_{\text{eff}}^2/2}$, up to second order. Details of the calculation are found in Ref. 20, with the result being

$$W_{\text{eff}} = W\sqrt{1 - \frac{a^2/W^2}{e^{a^2/W^2} - 1}}. \tag{24}$$

For reference, the dependence of W_{eff} on W/a is illustrated in Fig. 5. When $W/a \to 0$, $W_{\text{eff}} \to W$, as expected. From Fig. 5, it is further seen that $W_{\text{eff}} \approx W$ for $W/a < 0.5$, in agreement with Ref. 20. For $W/a \to \infty$, $W_{\text{eff}} \to a/\sqrt{2}$, corresponding to the simple estimate of Ref. 30. This upper limit of W_{eff} represents the Gaussian approximation of the Airy disk diffraction pattern, where the beam spot size is only limited by diffraction from the circular aperture near the plasma,[20] defined by the port liner at W7-X.[7] For typical W7-X PCI parameters ($W = 40\,\text{mm}$, $a = 42\,\text{mm}$), $W_{\text{eff}} = 26.9\,\text{mm}$, and picking $k \approx 6\,\text{cm}^{-1}$, which is representative of the ion temperature gradient-driven modes with the highest linear growth rates in W7-X ECRH plasmas,[6] we find $\sqrt{2}/(kW_{\text{eff}}) = 5°$. These considerations motivated the choice of $\alpha = 5°$ as the minimum α employed at W7-X and in Fig. 4. We do, however, note that masks with $\alpha = 6°$, $7°$, and $45°$ have also been manufactured and tested at W7-X. Nevertheless, the $\alpha = 5°$ mask was used in most experiments during the first long-pulse experimental campaign,[24] as it provides the greatest degree of localization while allowing a significant fraction of the scattered beam spot power to pass in the most relevant k range. We, therefore, focus mainly on the $\alpha = 5°$ case in the following.

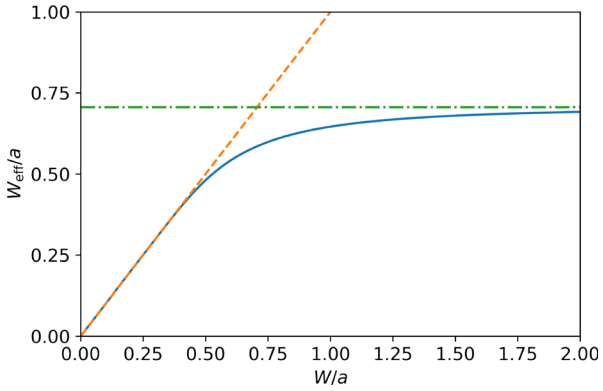

FIG. 5. $W_{\rm eff}/a$ vs W/a. In addition to $W_{\rm eff}/a$ based on Eq. (24) (solid line), we plot $W_{\rm eff} = W$ (dashed line) and $W_{\rm eff} = a/\sqrt{2}$ (dashed-dotted line). For Eq. (24), $W_{\rm eff} \approx W$ when $W/a < 0.5$ and $W_{\rm eff} \to a/\sqrt{2}$ for $W/a \to \infty$, in agreement with the results of Ref. 20.

In Appendix D, we compare the AC mask response function $\mathcal{M}_{\mathbf{k}} = m_0 m_{\mathbf{k}}$ obtained from Eqs. (19) and (22), using $W_{\rm eff}$ from Eq. (24) and $W_{\rm eff} = W$, with numerical evaluation of Eqs. (7) and (8) for an $\alpha = 5°$ mask. Based on this, we conclude that the approximate $\mathcal{M}_{\mathbf{k}}$ utilizing $W_{\rm eff}$ from Eq. (24) remains close to the numerical result even when $W/a \gg 1$, while the approximate $\mathcal{M}_{\mathbf{k}}$ utilizing $W_{\rm eff} = W$ is only close for $W/a < 0.5$, as expected from Fig. 5. We shall, therefore, use the approximate $\mathcal{M}_{\mathbf{k}}$ with $W_{\rm eff}$ from Eq. (24) for the analyses in the remainder of this paper.

Next, we compare the approximate $\mathcal{M}_{\mathbf{k}}$ with the full synthetic mask response based on Eq. (2). To facilitate comparison of the model with experimental data in Sec. IV, we compute the signal for a model W7-X sound wave calibration signal resembling that in Ref. 7. The sound wave calibration system at W7-X is designed to induce a known phase shift, ϕ, with a single dominant $\mathbf{k}$ and frequency component, allowing absolute calibration of the line-integrated $\tilde{n}_e$ and M measured by PCI.[4] Specifically, we investigate a ϕ of the form

$$\phi = -\phi_{\rm cal}(1 - Cx)\cos[k_s(x - v_s t)]. \tag{25}$$

Here, x is the coordinate along the quasi-poloidal measurement direction of the PCI detector arrays (cf. Fig. 1) with $x = 0$ at the beam center, t is a time coordinate, $\phi_{\rm cal} = 5.8 \times 10^{-3}$ and $C = 1.27\,{\rm m}^{-1}$ are obtained from a new sound wave pressure profile fit, $v_s = 343\,{\rm m/s}$ is the speed of sound, and k_s is the sound wave number. Details of the numerical evaluation of the full synthetic PCI signal in the presence of a mask are given in Appendix E. We use PCI parameters from the first long-pulse W7-X experimental campaign,[24] resembling those of Ref. 7, with the beam power at the detectors reduced to 700 mW, $a = 42\,{\rm mm}$, and $M = 3.3$. To compute the mask response from the synthetic PCI signal, we adopt the analysis technique that will also be used for the experimental results in Subsection IV A. We first compute the power spectral density (psd) of the PCI signal in (k_x, f) space, where k_x is the wave number along the x direction and f is the

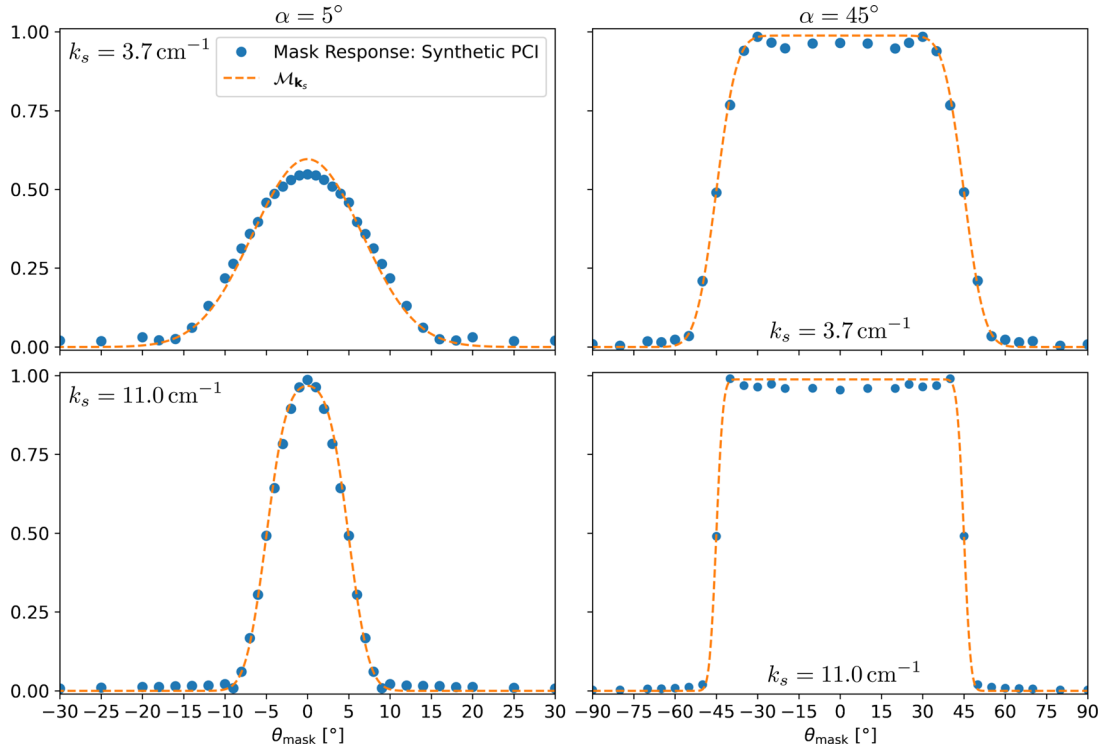

FIG. 6. Full synthetic PCI mask response from the model W7-X sound wave calibration signal (solid circles) and $\mathcal{M}_{k_s}$ (dashed lines) for $\theta = 0$, $W = 40\,{\rm mm}$, $a = 42\,{\rm mm}$, $k_{\rm min} = k_{\rm mask} = 1.6\,{\rm cm}^{-1}$, and $M = 3.3$. The left and right columns are obtained for $\alpha = 5°$ and 45°, respectively; the top and bottom rows utilize $k_s = 3.7\,{\rm cm}^{-1}$ and $11.0\,{\rm cm}^{-1}$, respectively.

frequency. Next, we integrate the psd over a region of (k_x, f) space around the peak due to the sound wave signal at $k_x = k_s$ and $f = k_s v_s/(2\pi)$. The mask response is finally found as the square root of the spectral power with the mask present divided by the spectral power without the mask, which mimics $\mathcal{M}_{\mathbf{k}}$ with $\mathbf{k} = \mathbf{k}_s = k_s \mathbf{e}_x$. In Fig. 6, we plot the synthetic PCI mask response obtained in this manner for $t \in [0, 1\,\mathrm{ms}]$ with a time resolution of $0.5\,\mu\mathrm{s}$ (typical values at W7-X[4,6]) and integration over $k_x \in [k_s - 5\,\mathrm{cm}^{-1}, k_s + 5\,\mathrm{cm}^{-1}]$ and $f \in [k_s v_s/(2\pi) - 3\,\mathrm{kHz}, k_s v_s/(2\pi) + 3\,\mathrm{kHz}]$, alongside $\mathcal{M}_{\mathbf{k}_s}$, vs θ_{mask}. The left column of Fig. 6 shows the results obtained for an $\alpha = 5^\circ$ mask, while the right column shows the results for an $\alpha = 45^\circ$ mask. Similarly, the top row of Fig. 6 shows the results for $k_s = 3.7\,\mathrm{cm}^{-1}$, mimicking the typical k_s at W7-X,[4] while the bottom row shows the results for $k_s = 11.0\,\mathrm{cm}^{-1}$, which is the largest k_s employed in the sound wave tests of Subsec. IV A. The approximate $\mathcal{M}_{\mathbf{k}_s}$ is seen to closely resemble the full synthetic PCI mask response in all cases. We particularly note that the widths of the transition regions around $\theta_{\mathrm{mask}} - \theta = \pm\alpha$ at different k_s are well described by the approximate $\mathcal{M}_{\mathbf{k}_s}$ with W_{eff} from Eq. (24). This indicates that the model captures the main effects of diffraction from the circular aperture within the Fraunhofer framework for typical W7-X parameters. Additionally, Fig. 6 indicates a mask response ≈ 0.5 when $\theta_{\mathrm{mask}} - \theta = \pm\alpha$ in a wide range of k_s, even for the full synthetic PCI signal; in Sec. IV, we confirm that this is also the case for the experimental PCI signal. This provides a useful metric for determining the localization region of a mask with a given α in W7-X.

Figure 7 shows the position of the upper and lower half-response curves ($\theta_{\mathrm{mask}} - \theta = \pm\alpha$, respectively), bounding the main response region of an $\alpha = 5^\circ$ mask, vs θ_{mask} in different magnetic configurations at W7-X.[31] θ is computed along the central PCI LoS (cf. Fig. 1), based on magnetic equilibria calculated using the VMEC code.[32] The radial position along the central PCI LoS in Fig. 7 is expressed using the normalized radial coordinate based on toroidal magnetic flux from VMEC, ρ_{tor}. ρ_{tor} is zero on the magnetic axis, one on the last closed

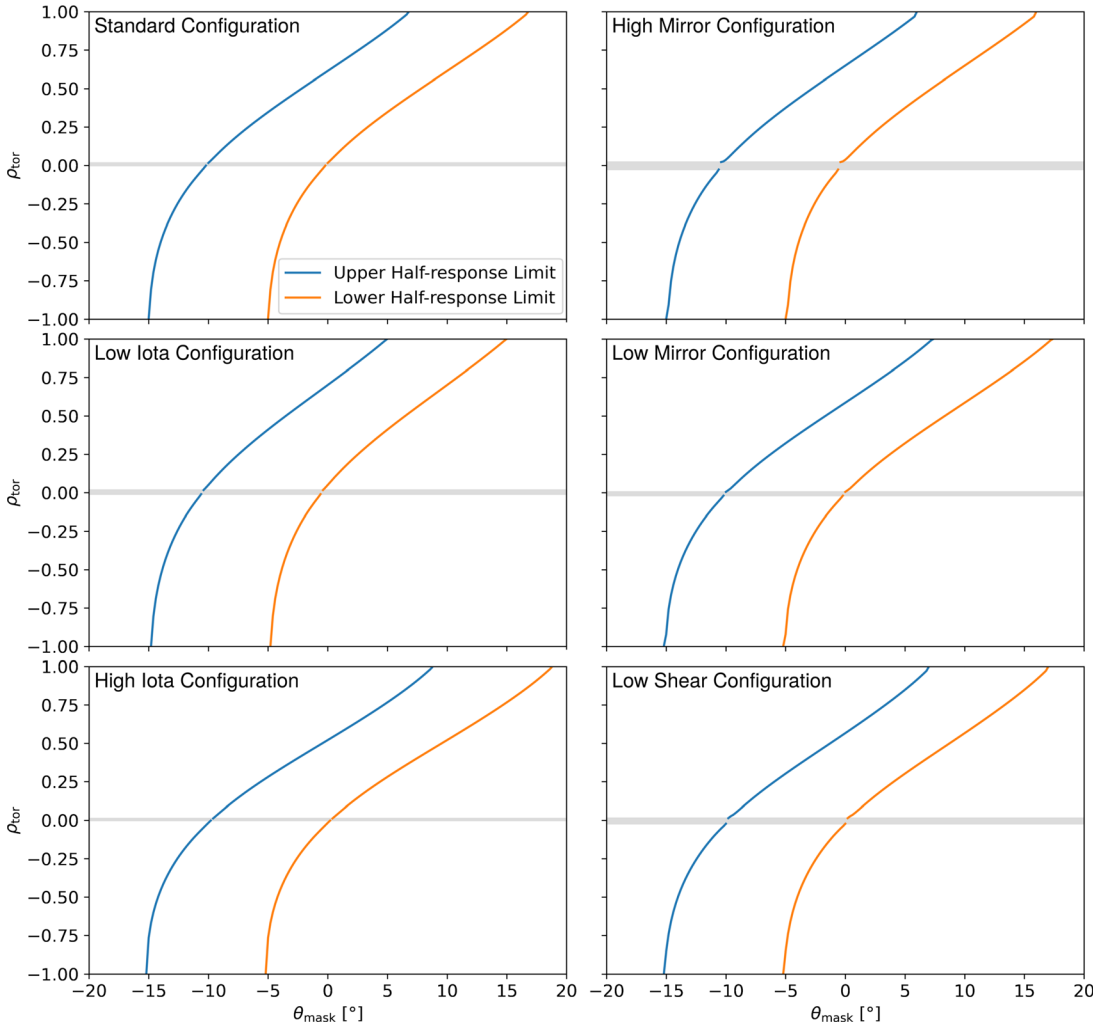

FIG. 7. Half-response curves, bounding the main response ρ_{tor} region of an $\alpha = 5^\circ$ mask, vs θ_{mask}. We use θ values along the central PCI LoS in different W7-X magnetic configurations. The central LoS does not reach the ρ_{tor} values in the gray shaded areas.

flux surface, and has a magnitude roughly proportional to the distance from the magnetic axis. We have further used a negative or positive sign of ρ_{tor} to indicate whether a position is on the inboard or outboard side of W7-X, respectively; as in Ref. 7, the switch from the inboard to the outboard side is taken to occur at the minimum of $|\rho_{\mathrm{tor}}|$. The gray shaded areas in Figs. 7 and 8 illustrate the region with $|\rho_{\mathrm{tor}}|$ below the minimum value reached by the central PCI LoS. From Fig. 7, it is clear that the half-response curves are relatively similar between the different magnetic configurations, with differences in the rotational transform (iota) being the main source of variation between the configurations, as expected based on Fig. 6 of Ref. 4. The standard, high mirror, low mirror, and low shear configurations all have similar iota values, and are consequently very similar in terms of their localization properties. The variation of θ on the outboard side of W7-X is slightly smaller in the low iota configuration, while it is slightly larger in the high iota configuration.

In Fig. 8, we plot $\mathcal{M}_{\mathbf{k}}$ of an $\alpha = 5^\circ$ mask at different θ_{mask} along the central PCI LoS for the W7-X standard magnetic configuration, with k_x values corresponding to $M = 3.3$. The k values used in Eq. (22) are computed from k_x, $k = |k_x/\cos(\theta)|$; this accurately reproduces the mask response from full synthetic PCI calculations, resembling Fig. 6, for $\theta \neq 0$. In all cases, no localization is obtained for $|k_x| < k_{\mathrm{mask}} = 1.6\,\mathrm{cm}^{-1}$, due to the central circular mask cutout. The relatively large angle covered by the scattered beam spots at low k (cf. Fig. 3) additionally limits the localization when $|k_x| \lesssim 5\,\mathrm{cm}^{-1}$. At larger $|k_x|$, an almost k-independent main response ρ_{tor} region is observed in Fig. 8, due to the constant mask α. The main response ρ_{tor} region depends on θ_{mask} as shown in the top left panel of Fig. 7. For $\theta_{\mathrm{mask}} = 15^\circ$ and -15°, the main signal is localized to the outboard and inboard side edge/scrape-off layer, respectively. When $\theta_{\mathrm{mask}} = 10^\circ$, the main signal is localized to the outer third of the outboard side. At $\theta_{\mathrm{mask}} = 5^\circ$, the main response is localized to mid radii on the outboard side, with a width close to half the minor radius, as expected from Fig. 7. For $\theta_{\mathrm{mask}} = 0^\circ$, the main response is localized to the inner half of the outboard side, while the width is similar to the $\theta_{\mathrm{mask}} = 5^\circ$ case. When $\theta_{\mathrm{mask}} = -2^\circ$, the main response is limited to the central part of the plasma, $\rho_{\mathrm{tor}} \in [-0.2, 0.5]$, but the width is increased relative to the $\theta_{\mathrm{mask}} = 0^\circ$ and 5° cases due to the small

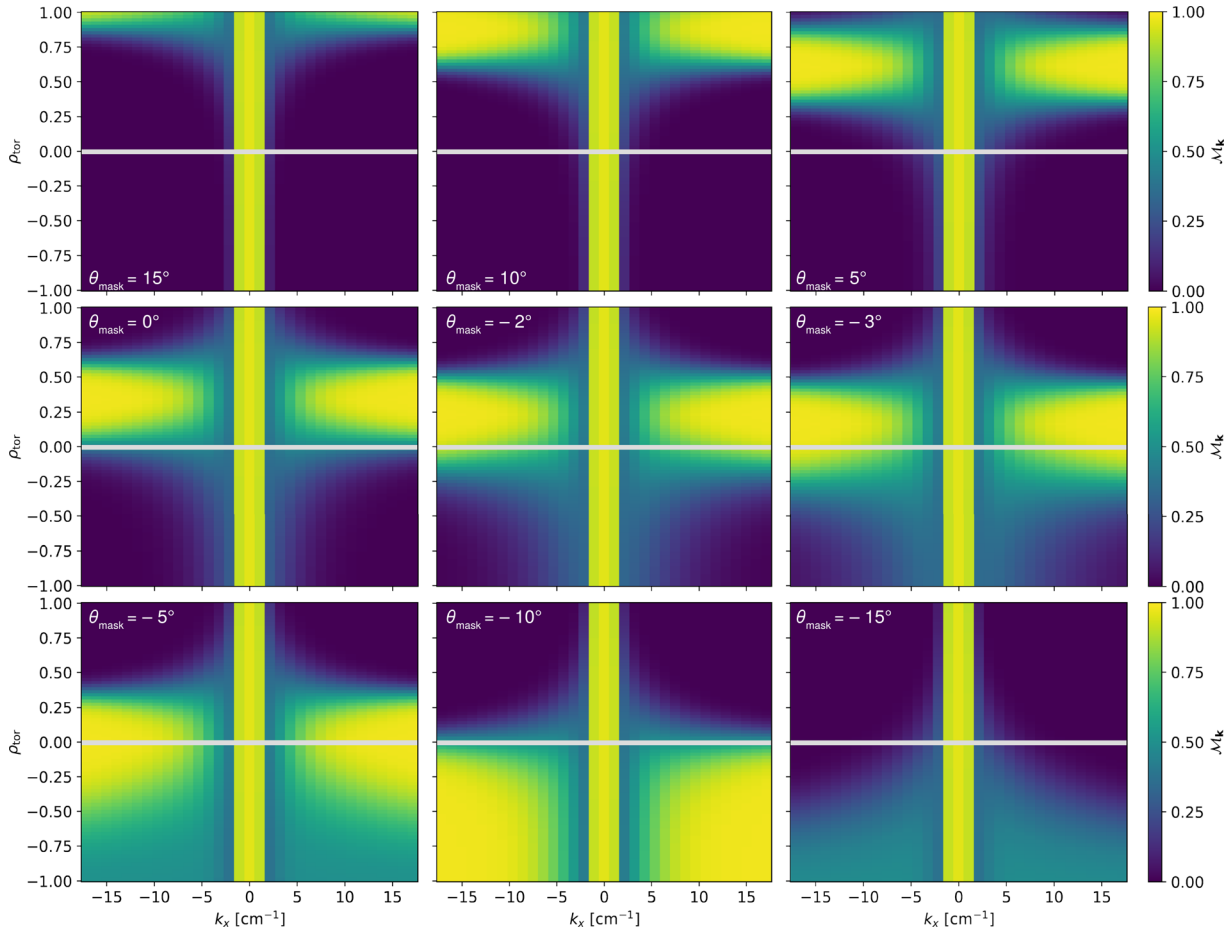

FIG. 8. $\mathcal{M}_{\mathbf{k}}$ for θ along the central PCI LoS at different θ_{mask}. The plots use an $\alpha = 5^\circ$ mask in the W7-X standard configuration with $W = 40\,\mathrm{mm}$, $a = 42\,\mathrm{mm}$, and $M = 3.3$. For $|k_x| < k_{\mathrm{mask}} = 1.6\,\mathrm{cm}^{-1}$, no localization is obtained due to the central circular mask cutout. At larger $|k_x|$, a nearly k-independent main response ρ_{tor} region is found, due to the constant mask α. The variation of the main response ρ_{tor} region with θ_{mask} is given by the top left panel of Fig. 7.

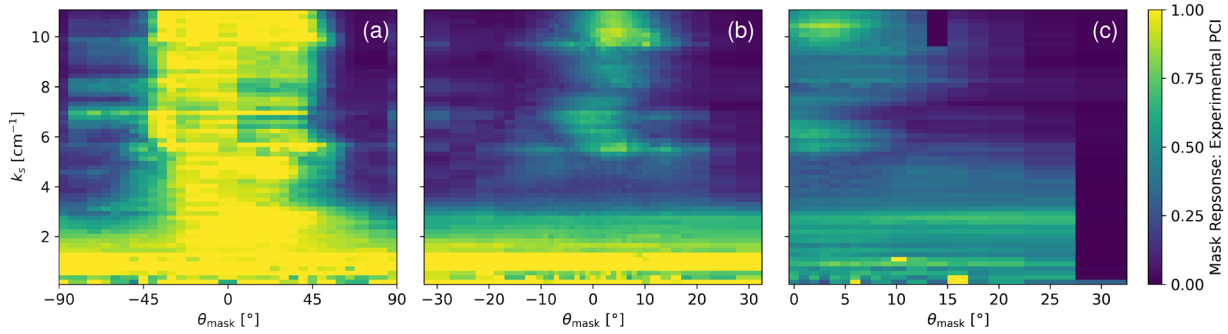

FIG. 9. Experimental mask response to the PCI sound wave calibration speaker at W7-X for different mask and beam parameters. Panel (a) has $\alpha = 45^\circ$ and a nominal $W = 40$ mm; panel (b) has $\alpha = 5^\circ$ and a nominal $W = 40$ mm; panel (c) has $\alpha = 5^\circ$ and a nominal $W = 20$ mm.

variation of θ on the inboard side of W7-X; this becomes more pronounced for $\theta_{\mathrm{mask}} = -3^\circ$. At $\theta_{\mathrm{mask}} = -5^\circ$, the response is negligible for $\rho_{\mathrm{mask}} < 0.25$, but remains significant over the entire inboard side due to the small θ variation, and finally for $\theta_{\mathrm{mask}} = -10^\circ$, the main response is localized to the inboard side.

The results from Figs. 7 and 8 allow interpretation of the experimental PCI mask results from W7-X in Sec. IV. We use $\mathcal{M}_{\mathbf{k}}$ profiles similar to the ones in Fig. 8 to compute (k_x, f) spectra in the presence of a mask with the synthetic PCI model from Ref. 7. The psd at each k_x value is calculated by weighing $\tilde{n}_e$ along the LoS with the $\mathcal{M}_{\mathbf{k}}$ at the k_x in question, running the synthetic PCI model of Ref. 7, and computing the psd at the relevant k_x. This procedure is repeated until the psd, weighed by $\mathcal{M}_{\mathbf{k}}$, is obtained for all k_x values.

IV. EXPERIMENTAL RESULTS

We discuss the experimental performance of the W7-X localization masks for three different cases. First, we consider the mask response obtained from the PCI sound wave calibration system with different mask and beam parameters. Next, the masks are used to confirm the location of the plasma turbulence features in standard W7-X ECRH plasmas expected based on Ref. 6. Finally, we demonstrate the new result that the masks allow the location of magnetohydrodynamic (MHD) modes with sufficiently large k to be inferred. All mask experiments discussed below were carried out with a mask placed in front of one detector array, while the other detector array operated simultaneously without a mask.

A. Mask response to the sound wave calibration signal

Figure 9 shows the experimental PCI mask response, obtained by scanning the sound wave speaker frequency from 1 to 60 kHz in increments of 1 kHz and applying the analysis technique used for the synthetic PCI signal in Fig. 6. At each frequency step, a 4 ms burst is launched from the speaker. The start of the bursts is separated by 50 ms to allow damping of the sound wave from the previous burst. Our analysis is carried out using the time intervals $1 - 2$ ms after the start of each burst to minimize the effects of transients when turning on the speaker and reflections from the mirror box where the speaker is located.[4] We have confirmed that comparable results are obtained using different time intervals as well as when the k_x and f regions used for computing the mask response are modified. Three combinations of mask and beam parameters are studied in Fig. 9. Panel (a) shows the results for an $\alpha = 45^\circ$ mask and a nominal $W = 40$ mm beam. Panels (b) and (c) show the results for an $\alpha = 5^\circ$ mask, with a nominal $W = 40$ and 20 mm, respectively. Different W were obtained by modifying the size of the injected beam, using a telescope with variable magnification between the PCI laser and the plasma.[4] While the features in Fig. 9 are generally similar to those expected based on $\mathcal{M}_{\mathbf{k}_s}$, with $\theta = 0$, $a = 42$ mm, and $k_{\mathrm{mask}} = 1.6\,\mathrm{cm}^{-1}$, seen in Fig. 10, clear differences are visible as well. Some differences can be explained by non-ideal properties of the calibration sound wave. For instance, the response center of the $\alpha = 5^\circ$ mask in Fig. 9 has a changing θ_{mask}, e.g., seen around $k_s \in [5\,, 6\,\mathrm{cm}^{-1}]$, indicating that the θ of the sound wave

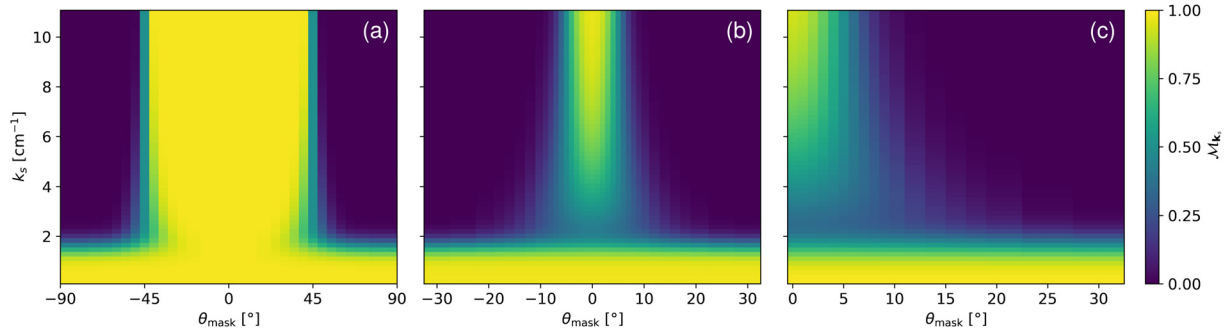

FIG. 10. Idealized mask response to the PCI sound wave calibration speaker at W7-X, given by $\mathcal{M}_{\mathbf{k}_s}$ with $\theta = 0$, $a = 42$ mm, and $k_{\mathrm{mask}} = 1.6\,\mathrm{cm}^{-1}$. Panel (a) has $\alpha = 45^\circ$ and $W = 40$ mm; panel (b) has $\alpha = 5^\circ$ and $W = 40$ mm; panel (c) has $\alpha = 5^\circ$ and $W = 20$ mm.

emitted by the speaker varies with k_s. Similarly, the mask response has a lower maximum value for $k_s \in [7\,\mathrm{cm}^{-1}, 10\,\mathrm{cm}^{-1}]$, and is significantly wider at $k_s \approx 7$, 8, and $10\,\mathrm{cm}^{-1}$, than for other comparable k_s values in all cases. It, thus, appears that these features also originate from the behavior of the sound wave calibration speaker, which is for instance known to display side lobes at certain k_s. The broad mask response for $k_s < k_{\mathrm{min}} = k_{\mathrm{mask}} = 1.6\,\mathrm{cm}^{-1}$ further shows different levels in panel (c), compared with panels (a) and (b) of Fig. 9. This may be explained by the low PCI signal strength due to the lack of phase contrast for $k_s < k_{\mathrm{min}}$, which invalidates the assumptions made in the simplified mask model and results in a low signal-to-noise ratio. There are, however, some differences between Figs. 9 and 10, which appear to be of a more fundamental nature. One difference is that the experimental transition regions are wider than the ones expected based on $\mathcal{M}_{\mathbf{k}_s}$. This appears to be the case for the transition region around $k_s = k_{\mathrm{mask}} = 1.6\,\mathrm{cm}^{-1}$, but is most clearly seen in the width of the mask response at high k_s values. The mask response at $k_s = 11.0\,\mathrm{cm}^{-1}$ can, e.g., be fitted by a function of the form of $\mathcal{M}_{\mathbf{k}_s}$ with $W_{\mathrm{eff}} = 10.3$, 12.1, and 9.4 mm in panels (a)–(c) of Fig. 9, respectively; Eq. (24) yields $W_{\mathrm{eff}} = 26.9$ mm for panels (a) and (b) and $W_{\mathrm{eff}} = 19.45$ mm for panel (c), using the nominal parameters from Fig. 10. This may be partially due to the PCI laser beam having non-Gaussian features as well as a slightly non-optimal location of the PCI localization masks during the first long-pulse W7-X experimental campaign,[24] which will be improved in future experimental campaigns. However, the large discrepancy also suggests that inclusion of diffraction effects beyond the Fraunhofer model used here may be necessary to accurately describe the width of the mask response, in agreement with earlier sound wave measurements at DIII-D.[18] Since the best-fitting W_{eff} is significantly different in panels (a) and (b) of Fig. 9, despite the beam parameters being nominally equal, a simple replacement W_{eff} to account for additional diffraction cannot be derived based on the experimental data. We do, however, note that the ratio between the best-fitting W_{eff} in panels (b) and (c) is relatively close to that expected based on Eq. (24), which is consistent with a similar ratio between the beam spot sizes. A final notable difference between Figs. 9 and 10 is that a localized mask response with the $\alpha = 5^\circ$ mask, used in panels (b) and (c), is obtained for $k_s \gtrsim 5\,\mathrm{cm}^{-1}$ and $k_s \gtrsim 3\,\mathrm{cm}^{-1}$, respectively. A localized response at lower k_s appears to be feasible for the $\alpha = 45^\circ$ mask from panel (a) of Fig. 9. This may, therefore, be a consequence of diffraction effects beyond the Fraunhofer model preventing localized measurements due to the small mask opening at low k_s for the $\alpha = 5^\circ$ mask. Despite the differences between Figs. 9 and 10, we note that the width of the main response ($\mathcal{M}_{\mathbf{k}_s} > 0.5$) region for the k_s values with a localized response is $\approx 2\alpha$ in all cases. This indicates that the basic localization properties from Fig. 7 are reproduced and may be used to interpret the experimental results.

B. Localization of plasma turbulence features

We now turn to the application of the PCI localization masks to actual plasma programs at W7-X. Figure 11 shows (k_x, f) spectra from plasmas heated by 4 MW of ECRH in the W7-X standard configuration from the first long-pulse experimental campaign.[24] The left and middle panels of Fig. 11 show the psd obtained in the same time interval from the detector without a mask and the detector covered by an $\alpha = 5^\circ$ mask set to $\theta_{\mathrm{mask}} = 5^\circ$ (main response $\rho_{\mathrm{tor}} \in [0.3, 0.8]$), respectively. The right panel shows the psd from a similar time point in the subsequent experimental program, where the $\alpha = 5^\circ$ mask is set to $\theta_{\mathrm{mask}} = -2^\circ$ (main response $\rho_{\mathrm{tor}} \in [-0.2, 0.5]$). In all cases, the signals at small $|k_x|$ are similar, indicating the limited ability of the masks to localize the PCI signal in this region, as expected. When the mask is set to $\theta_{\mathrm{mask}} = 5^\circ$, the psd at larger positive k_x is significantly reduced compared to the psd without the mask, while the psd at larger negative k_x is only slightly reduced. With the mask set to $\theta_{\mathrm{mask}} = -2^\circ$, the signal is significantly reduced at all larger $|k_x|$.

This can be understood based on the $\mathcal{M}_{\mathbf{k}}$ of Fig. 8 and the overlap of the main mask response regions with the dominant turbulence features from Ref. 6, shown in Fig. 12. According to Ref. 6 and as illustrated in Fig. 12, the main PCI turbulence features originate around the well of the neoclassical E_r, corresponding to the regions $|\rho_{\mathrm{tor}}| \in [0.6, 0.8]$. The features at negative/positive k_x originate from the outboard/inboard side of the PCI LoS for the usual $\mathbf{B}$ direction at W7-X, respectively. When $\theta_{\mathrm{mask}} = 5^\circ$, the mask response at larger $|k_x|$ is strongest around $\rho_{\mathrm{tor}} \in [0.3, 0.8]$, covering the neoclassical E_r well on the outboard side, as seen in the middle panel of Fig. 12. This is consistent with the psd at larger negative k_x being similar to the case without the mask, while the psd at larger positive k_x is significantly reduced, as seen in Fig. 11. It is further supported by the rotation direction of the PCI features being opposite in plasmas with reversed $\mathbf{B}$ (not shown). On the other hand, when $\theta_{\mathrm{mask}} = -2^\circ$, the mask response at larger $|k_x|$ is strongest for $\rho_{\mathrm{tor}} \in [-0.2, 0.5]$, which is outside the neoclassical E_r wells, as seen in the right panel of Fig. 12. Consequently,

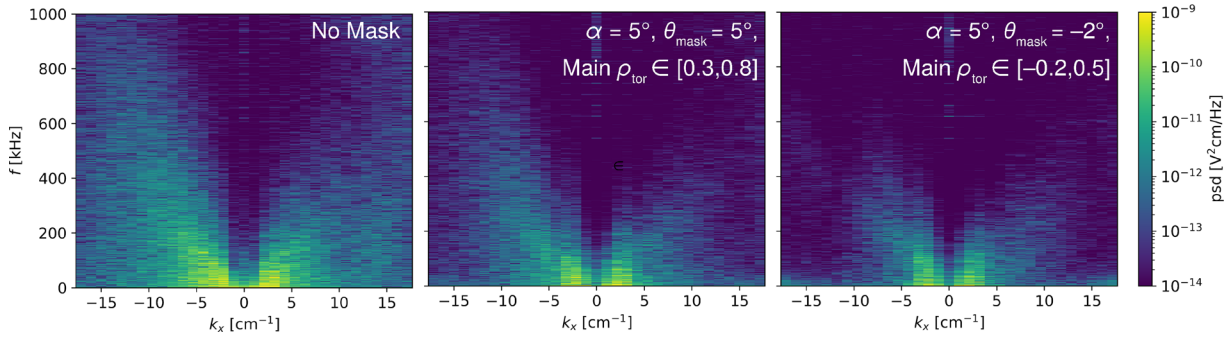

FIG. 11. Experimental (k_x, f) spectra at W7-X. The no mask case (left panel) and $\alpha = 5^\circ$, $\theta_{\mathrm{mask}} = 5^\circ$ case (middle panel, main response $\rho_{\mathrm{tor}} \in [0.3, 0.8]$) are taken from the same interval, experiment time $\in$ [11 s, 11.001 s], of program 20 230 323.062. The $\alpha = 5^\circ$, $\theta_{\mathrm{mask}} = -2^\circ$ case (right panel, main response $\rho_{\mathrm{tor}} \in [-0.2, 0.5]$) is from the same interval of the subsequent program.

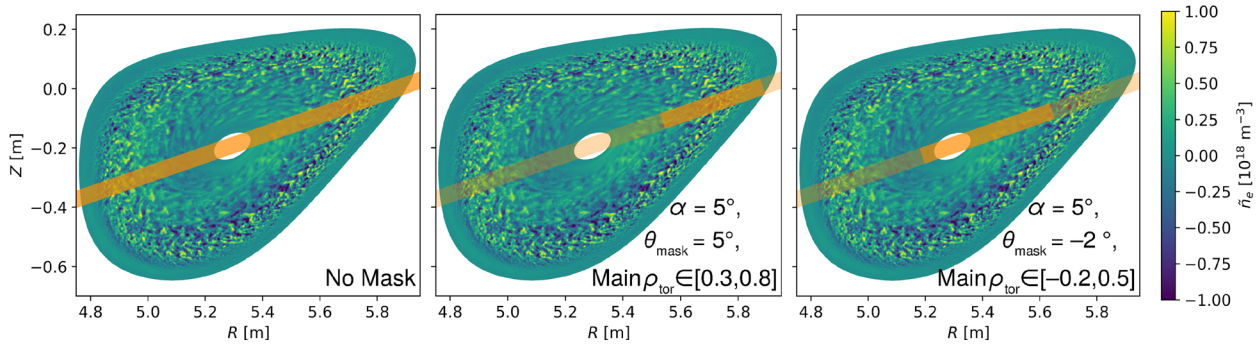

FIG. 12. $\tilde{n}_e$ associated with the turbulence from Ref. 6 (at $t = 0$) in cylindrical (R, Z) coordinates. The orange shaded area in the left panel indicates the region of the full PCI LoSs, while the darker shaded areas in the middle and right panels indicate the main response regions in the $\alpha = 5°$, $\theta_{\text{mask}} = 5°$ and $\alpha = 5°$, $\theta_{\text{mask}} = -2°$ cases, respectively. Note that $\tilde{n}_e$ only covers $|\rho_{\text{tor}}| \in [0.1, 0.9]$.[33]

the psd is significantly reduced at all large $|k_x|$ compared to that of the detector without a mask, in agreement with Fig. 11.

The qualitatively similar behavior noted above further agrees with synthetic PCI results based on the simplified turbulence model used in Ref. 6, weighed by the $\mathcal{M}_{\mathbf{k}}$ from Fig. 8. Figure 13 shows synthetic (k_x, f) spectra with mask settings that mimic those of Fig. 11. The $\tilde{n}_e$ used for computing Fig. 13 is obtained by rotating the $\tilde{n}_e$ from Fig. 12, which is a single time point of a gyrokinetic simulation,[33] by a velocity field due to a neoclassical E_r. Details of the model are given in Appendix B of Ref. 6. Figure 13 reproduces the behavior of Fig. 11, indicating that the interpretation of Fig. 11 is consistent with the results obtained from synthetic PCI. We further note that the synthetic PCI results are similar to the experimental ones with the $\alpha = 5°$ mask in the W7-X standard configuration for $\theta_{\text{mask}} \leq 15°$. When $\theta_{\text{mask}} \in]15°, 25°]$, the experimental psd is larger than that expected from synthetic PCI. This may be attributed to the $\tilde{n}_e$ from Fig. 12 only covering $|\rho_{\text{tor}}| < 0.9$,[33] which is outside the main mask response region at larger $|k_x|$ for $\theta_{\text{mask}} > 15°$ (cf. Fig. 8). It does, however, also indicate that a non-negligible PCI signal may originate from the outboard scrape-off layer.

C. Localization of MHD modes

Having confirmed the location of the main PCI turbulence features from Ref. 6, we finally turn to a novel issue, namely, the possibility of inferring the location of coherent MHD modes aided by the PCI masks. Investigations of Alfvén eigenmodes using PCI have been carried out in Alcator C-Mod[34–36] and similar observations have been reported in W7-X.[3,4,11,12] Such modes generally possess $k < k_{\text{min}}, k_{\text{mask}}$,[34–36] meaning that the PCI masks are typically not capable of locating them. The masks do, nevertheless, have an impact on the ability of the PCI system to detect low-k MHD modes, as the reduced psd of the turbulence features in the presence of the masks generally makes the MHD modes more prominent relative to the non-MHD-related signal. However, in some cases, coherent modes with higher k values, for which localization is possible using the PCI masks, do occur. We note that the possibility of locating high-k MHD modes with the PCI system augments the MHD mode detection capabilities at W7-X. The in-vessel Mirnov coil system[11,37–39] mainly allows detection and localization of low-k modes in the outer part of W7-X plasmas.[39] Although the soft x-ray system[11,40,41] can also locate core MHD modes using *ad hoc* mode models,[41–43] it is generally limited to $f < 100$ kHz,[38] which is not the case for the PCI system.

An example of a high-k mode observed by the W7-X PCI system with an $\alpha = 5°$ mask at $\theta_{\text{mask}} = -2°$ (main response $\rho_{\text{tor}} \in [-0.2, 0.5]$) is seen in Fig. 14. Based on the (k_x, f) spectra in the left column of Fig. 14, the mode peaks around $f = 200$ kHz and $k_x = 4.3\,\text{cm}^{-1}$. The mode peak is at the edge of the k values for which the $\alpha = 5°$ mask allows localized measurements according to Fig. 9. This is confirmed by the right column of Fig. 14, showing mode k_x spectra, obtained by integrating the

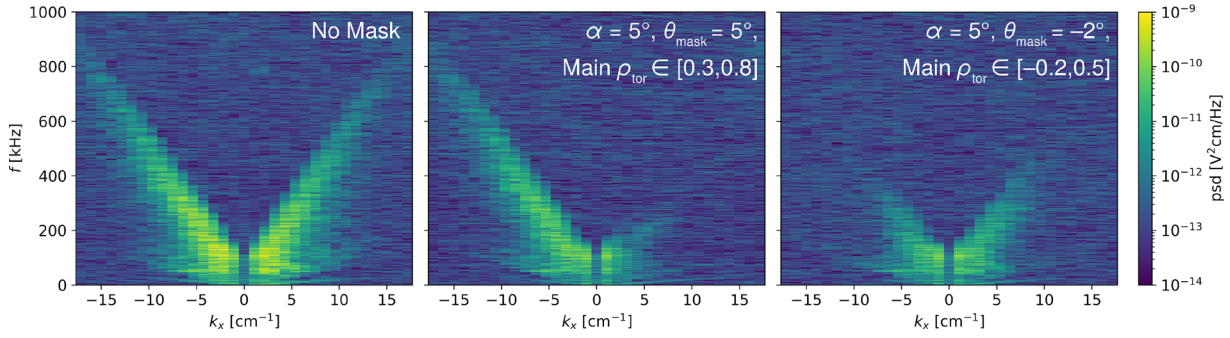

FIG. 13. Synthetic (k_x, f) spectra,[7] obtained by weighing the $\tilde{n}_e$ from Ref. 6 (cf. Fig. 12) by $\mathcal{M}_{\mathbf{k}}$, with $W = 40$ mm, $a = 42$ mm, and $M = 3.3$. The behavior is similar to that in Fig. 11.

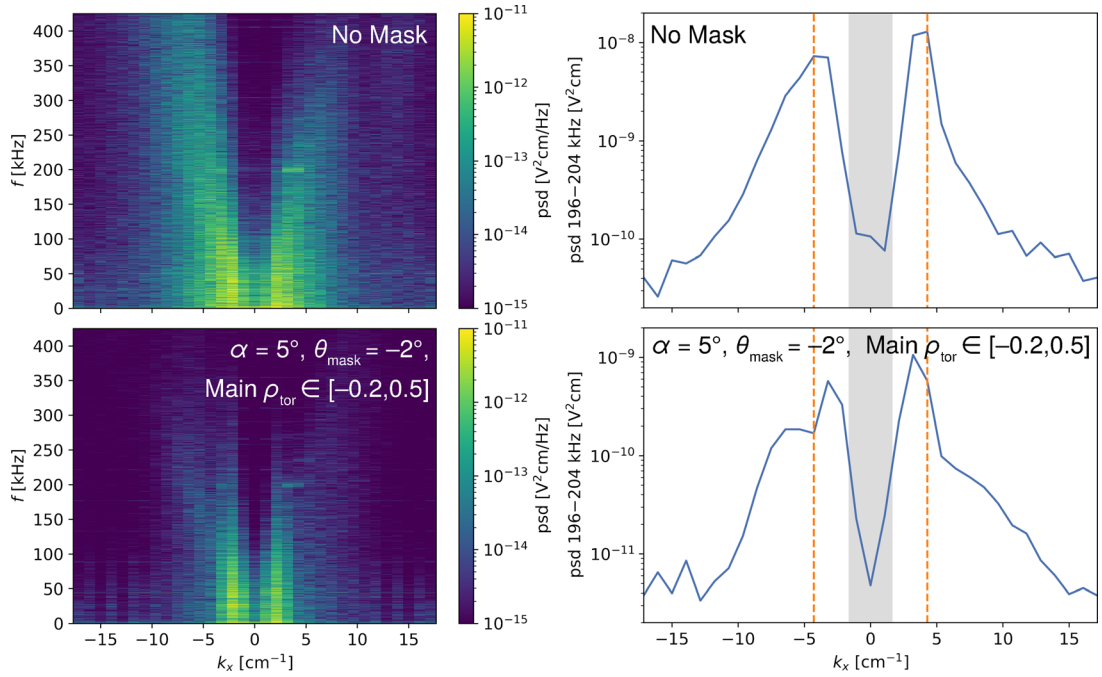

FIG. 14. Left: Experimental (k_x, f) spectra with a high-k MHD mode around $f = 200\,\text{kHz}$, $k_x = 4.3\,\text{cm}^{-1}$ from W7-X program 20 230 215.026, experiment time $\in [2.00\,\text{s}, 2.01\,\text{s}]$. Right: Mode k_x spectra (solid lines) obtained by integrating the psd from 196 to 204 kHz. $|k_x| < k_{\text{min}} = 1.6\,\text{cm}^{-1}$ (shaded areas) and the mode peaks at $|k_x| = 4.3\,\text{cm}^{-1}$ (dashed lines) are indicated.

psd over $f = 196 - 204\,\text{kHz}$. The mode psd in the presence of the mask decreases from $|k_x| = 3.2\,\text{cm}^{-1}$ to $|k_x| = 4.3\,\text{cm}^{-1}$, while the opposite is true without the mask, indicating that fluctuations from a smaller region of the plasma are imaged at $|k_x| = 4.3\,\text{cm}^{-1}$ compared with $|k_x| = 3.2\,\text{cm}^{-1}$. Overall, the mode psd at $k_x = 4.3\,\text{cm}^{-1}$ in the presence of the mask is $\sim 1/10$ of the value without the mask. Additionally, the mode psd at $k_x = 4.3\,\text{cm}^{-1}$ is enhanced by a factor of ≈ 2 relative to the mode psd at $k_x = -4.3\,\text{cm}^{-1}$ for the detector covered by the mask. The latter value is significant, as it can be taken as an indication of the relative suppression of the mode-related signal from the inboard and outboard sides caused by the mask, which is mainly determined by the location of the mode. Thus, by matching this ratio for synthetic PCI signals from models of the $\tilde{n}_e$ associated with modes at different locations, possible mode locations can be inferred. By also matching the overall suppression of the mode psd at $k_x = 4.3\,\text{cm}^{-1}$ in the presence of the mask, the possible locations of the mode may be further constrained. We show (k_x, f) spectra and related mode k_x spectra obtained through such matching in Fig. 15, along with the model mode $\tilde{n}_e$ used at $t = 0$ in Fig. 16. To allow the study of modes at various locations, we employed a simple *ad hoc* mode model, similar to the ones in Refs. 41–43, which is described in Appendix F. Based on this, a mode centered at $|\rho_{\text{tor}}| = 0.7$, rotating in the clockwise direction is inferred. The rotation velocity is similar to that of the turbulent fluctuations at $|\rho_{\text{tor}}| = 0.7$ due to the neoclassical E_r, meaning that the features at positive/negative k_x in Fig. 15 originate from the inboard/outboard side, respectively. Thus, the mode signal from the inboard side (positive k_x, $\rho_{\text{tor}} \approx -0.7$) is less suppressed by the mask than the signal from the outboard side (negative k_x, $\rho_{\text{tor}} \approx 0.7$), despite originating further from the main mask response region of $\rho_{\text{tor}} \in [-0.2, 0.5]$. This is caused by the small variation of θ on the inboard side, resulting in a noticeably larger $\mathcal{M}_{\mathbf{k}}$ for the $|k_x| = 4.3\,\text{cm}^{-1}$ mode near $\rho_{\text{tor}} = -0.7$ compared with $\rho_{\text{tor}} = 0.7$, as indicated by Fig. 8 and the shading of the PCI LoS in Fig. 16. It is, therefore, essential to account for the shape of $\mathcal{M}_{\mathbf{k}}$ when inferring the location of an MHD mode using a mask, rather than simply relying on the rough indication given by the main response region.

We note that without matching the reduction of the overall signal at $k_x = 4.3\,\text{cm}^{-1}$ in the presence of the mask, a mode centered at $\rho_{\text{tor}} = 0.35$ rotating in the counterclockwise direction would also be possible. For such a mode, the psd at $k_x = 4.3\,\text{cm}^{-1}$ integrated over $f = 196 - 204\,\text{kHz}$ would, however, be $\sim 1/3$ of the value without the mask, rather than the observed value of $\sim 1/10$. This illustrates how ambiguous mode locations may be resolved by requiring multiple ratios to match simultaneously, which is only achieved by the mode centered at $|\rho_{\text{tor}}| = 0.7$ rotating in the clockwise direction. Further constraints on the mode properties may be provided by implementing the ability to scan θ_{mask} during a plasma discharge. To obtain quantitative agreement between Figs. 14 and 15, more realistic mode $\tilde{n}_e$ and mask models would be required.

V. CONCLUSION AND OUTLOOK

We have investigated the impact of PCI localization masks theoretically and experimentally at W7-X. The masks are placed in a focal plane and only allow signals with $\mathbf{k}$ in a limited angular range to reach the PCI detectors. This can be mapped to signals from particular parts of the PCI LoS by noting that the $\mathbf{k}$ observed by PCI can be assumed to be almost perpendicular to $\mathbf{B}$ and the PCI LoS. In the Fraunhofer

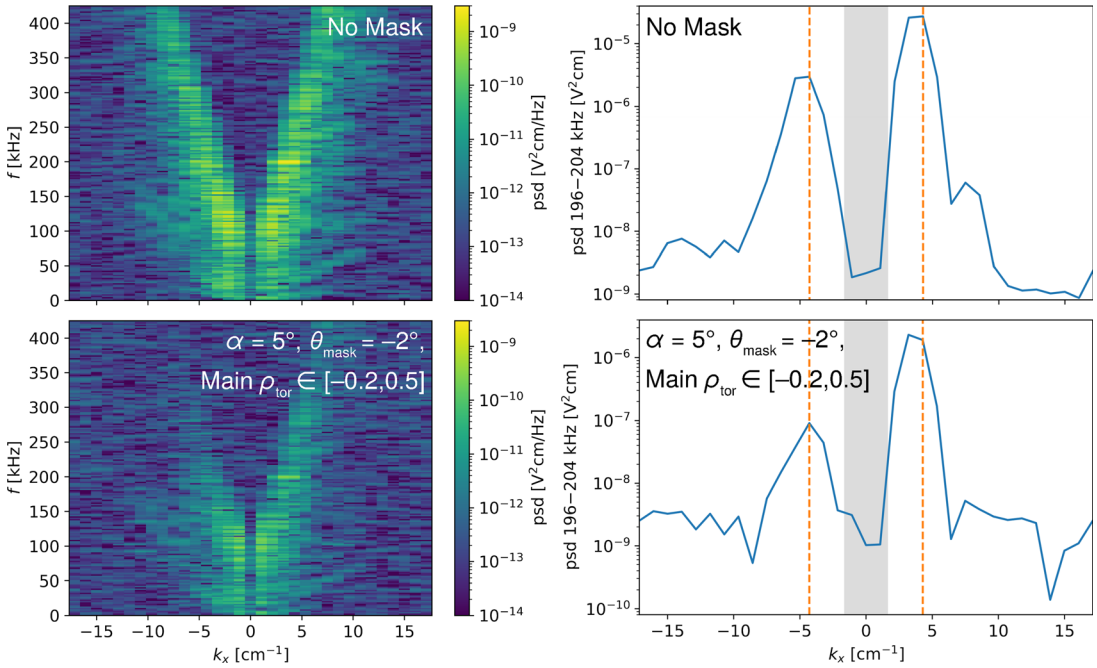

FIG. 15. Left: Synthetic (k_x, f) spectra with a high-k MHD mode, using $f_{MHD} = 200$ kHz, $a_0 = 0.0025$, $w = 0.05$, $\rho_0 = 0.7$, $m = -130$, $\theta_0^* = 0$, and $t \in [0, 0.5\,\text{ms}]$ in the model of Appendix F. Right: Mode k_x spectra (solid lines) obtained by integrating the psd from 196 to 204 kHz. $|k_x| < k_{min} = 1.6\,\text{cm}^{-1}$ (shaded areas) and the mode peaks at $|k_x| = 4.3\,\text{cm}^{-1}$ (dashed lines) are indicated.

diffraction framework, used by current synthetic PCI models,[7,15] we have demonstrated analytically that the PCI signal component at **k** in the presence of a mask can be fitted by multiplying the signal without a mask by $\mathcal{M}_{\mathbf{k}} = m_0 m_{\mathbf{k}}$. Here, $m_{\mathbf{k}}$ is the ratio of power in the **k** component at the detectors with and without the mask, while m_0 is the same quantity for the $k = 0$ component. These novel insights enabled the design of masks with specific localization properties and the interpretation of experimental mask results from the W7-X PCI system. The W7-X masks are designed to allow the $k = 0$ component to pass,

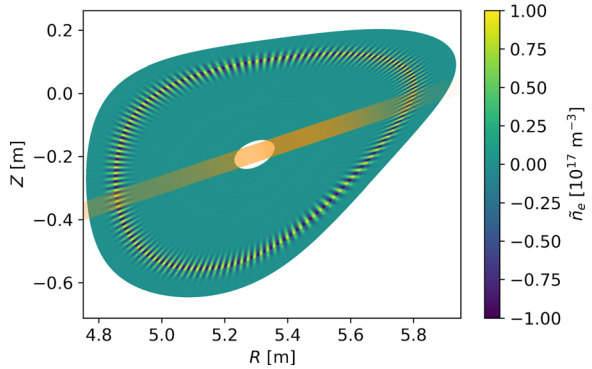

FIG. 16. $\tilde{n}_e$ associated with the MHD mode used for computing Fig. 15 (at $t = 0$) in cylindrical (R, Z) coordinates. The orange shaded area illustrates the region of the PCI LoSs in Fig. 15, with darker shaded areas indicating higher $\mathcal{M}_{\mathbf{k}}$ for a mode with $|k_x| = 4.3\,\text{cm}^{-1}$ at mask settings of $\alpha = 5°$, $\theta_{mask} = -2°$. Note that $\tilde{n}_e$ only covers $|\rho_{tor}| \in [0.1, 0.9]$.

i.e., have $m_0 \approx 1$, through a central circular cutout, covering the **k** region without phase contrast due to the finite width of the PCI phase plate groove. Outside the central cutout, the mask openings cover a fixed angular range of half-width α, allowing a specific region along the PCI LoS to be imaged for the **k** region, which is well resolved by the PCI system. As shown by the analytical model for an effective Gaussian beam in Appendix B, this mask design provides the least variation of the mask response region for different k values, simplifying the interpretation of the results obtained in the presence of the mask. Due to the small variation of the pitch angle of **B** at W7-X, the minimum beam spot size limits the possible resolution that may be obtained using the mask. On the outboard side, the minimum resolution is roughly half the minor radius for typical ion-scale turbulence k values, while the resolution on the inboard size is very limited in all cases.[20] This information has been used to select the minimum mask $\alpha = 5°$, which results in the localization characteristics listed above in all commonly employed W7-X configurations. The simplified mask model developed in this paper has been benchmarked against a full synthetic PCI calculation for the W7-X sound wave calibration signal,[7] confirming that it accurately captures the effect of the mask in the Faunhofer diffraction framework. One point of note is that the minimum focal plane beam spot size imposed by diffraction from the port liner near the plasma at W7-X[7,20] is recovered by the simplified model using an effective Gaussian beam approximation. Comparing the theoretical sound wave mask response with measurements shows that the qualitative features are reproduced. The experimental width of the transition regions around the edges of the mask openings is, however, significantly wider than the theoretical one. This may be partially attributed to non-Gaussian PCI laser beam features and a slightly

non-optimal position of the localization masks during the first long-pulse W7-X experimental campaign,[24] which will be improved in future experimental campaigns. However, the significant difference also indicates that diffraction effects beyond the Fraunhofer model may be required to obtain quantitative agreement, as previously found for the sound wave calibration system at DIII-D.[18] Nevertheless, the simplified model permits interpretation of PCI mask results from the first long-pulse W7-X experimental campaign[24] when combined with the W7-X synthetic PCI diagnostic.[7] We have specifically confirmed that the PCI signal in standard ECRH plasmas originates mainly from the neoclassical E_r well around $|\rho_{\mathrm{tor}}| \in [0.6, 0.8]$, in agreement with Refs. 6 and 7. Furthermore, we have presented the first results showing that PCI mask measurements, combined with synthetic PCI modeling, may allow localization of high-k coherent modes.

Several open lines inquiry remain following the present study. First, an extension of the mask response and synthetic PCI models beyond the Fraunhofer framework would facilitate quantitative comparisons between experimental and synthetic PCI signals including a mask. While a full scalar diffraction model was used to determine the sound wave mask response in Ref. 18, synthetic PCI investigations of plasmas have, to our knowledge, always relied on the Fraunhofer model.[7,14,15,25] An examination of the limits of the Fraunhofer model in the context of synthetic PCI, thus, appears to be warranted. Additionally, it would be of interest to explore the possibility of extending the novel simplified mask model presented for the Fraunhofer framework in this paper to more realistic diffraction models. Next, a more detailed experimental and synthetic PCI investigation of the results obtained using the masks at W7-X should be carried out. This could include systematic studies of differences in the PCI signal from the detectors with and without a mask as well as studies of the synthetic PCI signal with a mask from self-consistent turbulence and MHD models. We note that a mask has already been used to study changes in core turbulence during impurity seeding at W7-X.[44] Finally, it will be of interest to extend the W7-X PCI localization capabilities. This will be done by allowing scans of θ_{mask} during a plasma discharge, thus providing information about the turbulence and MHD mode characteristics in different regions of the same plasma. Comparisons of the PCI localization properties inferred using a scanning one-channel detector[22] and the masks will further be carried out to this end.

ACKNOWLEDGMENTS

We thank C. Büschel for providing valuable comments on an early version of this paper. The support for the MIT and SUNY-Cortland participation was provided by the U.S. Department of Energy, Grant No. DE-SC0014229. This work has been carried out within the framework of the EUROfusion Consortium, funded by the European Union via the Euratom Research and Training Programme (Grant Agreement No. 101052200–EUROfusion). The views and opinions expressed are, however, those of the authors only and do not necessarily reflect those of the European Union or the European Commission. Neither the European Union nor the European Commission can be held responsible for them.

AUTHOR DECLARATIONS

Conflict of Interest

The authors have no conflicts to disclose.

Author Contributions

S. K. Hansen: Formal analysis (lead); Funding acquisition (supporting); Investigation (lead); Methodology (equal); Software (equal); Validation (lead); Visualization (lead); Writing – original draft (lead); Writing – review & editing (equal). **M. Porkolab:** Funding acquisition (lead); Project administration (lead); Supervision (lead); Writing – review & editing (equal). **J.-P. Bähner:** Funding acquisition (supporting); Investigation (equal); Methodology (equal); Software (equal); Writing – review & editing (equal). **A. von Stechow:** Funding acquisition (supporting); Investigation (equal); Resources (equal); Software (equal); Writing – review & editing (equal). **O. Grulke:** Funding acquisition (equal); Project administration (equal); Resources (equal); Supervision (equal). **E. M. Edlund:** Funding acquisition (equal); Project administration (equal). **The W7-X Team:** Resources (equal).

DATA AVAILABILITY

Raw data were generated at the Wendelstein 7-X large-scale facility. Derived data supporting the findings of this study are available from the corresponding author upon reasonable request.

APPENDIX A: FIT COEFFICIENTS FOR THE SIMPLIFIED MASK MODEL

We perform a least squares fit of Eq. (6) to Eq. (5) by computing the absolute square of their difference and integrating the difference over the scaled image plane,

$$\begin{aligned}
&\int_{\mathrm{all}\,\mathbf{x}_\perp} |\mathbf{E}_{\mathrm{im}} - \mathbf{E}_{\mathrm{fit}}|^2 \, \mathrm{d}\mathbf{x}_\perp \\
&\quad \approx \rho \int_{\mathrm{all}\,\mathbf{x}_\perp} |\mathcal{F}^{-1}[\mathcal{P}_m \mathcal{F}(\mathcal{P}_a \mathbf{E}_0)] - m_0 \mathcal{P}_a \mathbf{E}_0|^2 \, \mathrm{d}\mathbf{x}_\perp \\
&\qquad + |A|^2 \int_{\mathrm{all}\,\mathbf{x}_\perp} \{ |\mathcal{F}^{-1}\left[\mathcal{P}_m \mathcal{F}(\mathcal{P}_a \mathbf{E}_0)(\mathbf{k}' - \mathbf{k})\right] \\
&\qquad - m_{\mathbf{k}} \mathcal{P}_a \mathbf{E}_0 \, \mathrm{e}^{\mathrm{i}\mathbf{k}\cdot\mathbf{x}_\perp}|^2 + |\mathcal{F}^{-1}\left[\mathcal{P}_m \mathcal{F}(\mathcal{P}_a \mathbf{E}_0)(\mathbf{k}' + \mathbf{k})\right] \\
&\qquad - m_{\mathbf{k}} \mathcal{P}_a \mathbf{E}_0 \, \mathrm{e}^{-\mathrm{i}\mathbf{k}\cdot\mathbf{x}_\perp}|^2 \} \, \mathrm{d}\mathbf{x}_\perp .
\end{aligned} \tag{A1}$$

The approximation on the right hand side of Eq. (A1) is obtained since $\mathcal{F}^{-1}[\mathcal{P}_m \mathcal{F}(\mathcal{P}_a \mathbf{E}_0)(\mathbf{k}' \mp \mathbf{k})] - m_{\mathbf{k}} \mathcal{P}_a \mathbf{E}_0 \, \mathrm{e}^{\pm \mathrm{i}\mathbf{k}\cdot\mathbf{x}_\perp}$ are roughly $\propto \mathrm{e}^{\pm \mathrm{i}\mathbf{k}\cdot\mathbf{x}_\perp}$, such that the cross terms are oscillatory functions of $\mathbf{x}_\perp$, which approximately vanish upon integration over the scaled image plane. We can now calculate the derivative of $\int_{\mathrm{all}\,\mathbf{x}_\perp} |\mathbf{E}_{\mathrm{im}} - \mathbf{E}_{\mathrm{fit}}|^2 \, \mathrm{d}\mathbf{x}_\perp$ with respect to m_0,

$$\begin{aligned}
\frac{\partial}{\partial m_0} \int_{\mathrm{all}\,\mathbf{x}_\perp} |\mathbf{E}_{\mathrm{im}} - \mathbf{E}_{\mathrm{fit}}|^2 \, \mathrm{d}\mathbf{x}_\perp = 2\rho \Bigg\{ m_0 \int_{\mathrm{all}\,\mathbf{x}_\perp} |\mathcal{P}_a \mathbf{E}_0|^2 \, \mathrm{d}\mathbf{x}_\perp \\
- \frac{1}{(2\pi)^2} \int_{\mathrm{all}\,\mathbf{k}'} \mathcal{P}_m |\mathcal{F}(\mathcal{P}_a \mathbf{E}_0)|^2 \, \mathrm{d}\mathbf{k}' \Bigg\},
\end{aligned} \tag{A2}$$

where we have made use of the following identity (and its complex conjugate)

$$\int_{\text{all }\mathbf{x}_\perp} (\mathcal{P}_a\mathbf{E}_0)^* \cdot \mathcal{F}^{-1}[\mathcal{P}_m\mathcal{F}(\mathcal{P}_a\mathbf{E}_0)]\,\mathrm{d}\mathbf{x}_\perp = \frac{1}{(2\pi)^2}\int_{\text{all }\mathbf{k}'} \mathcal{P}_m\mathcal{F}(\mathcal{P}_a\mathbf{E}_0)\cdot\left[\int_{\text{all }\mathbf{x}_\perp}(\mathcal{P}_a\mathbf{E}_0)^*\,\mathrm{e}^{\mathrm{i}\mathbf{k}'\cdot\mathbf{x}_\perp}\,\mathrm{d}\mathbf{x}_\perp\right]\mathrm{d}\mathbf{k}' = \frac{1}{(2\pi)^2}\int_{\text{all }\mathbf{k}'}\mathcal{P}_m|\mathcal{F}(\mathcal{P}_a\mathbf{E}_0)|^2\,\mathrm{d}\mathbf{k}', \tag{A3}$$

resulting from the definitions of $\mathcal{F}^{-1}$ and $\mathcal{F}$. The value of m_0 for the least squares fit is found by setting Eq. (A2) equal to zero (since the derivative of Eq. (A2) with respect to m_0, $2\rho\int_{\text{all }\mathbf{x}_\perp}|\mathcal{P}_a\mathbf{E}_0|^2\,\mathrm{d}\mathbf{x}_\perp > 0$, the stationary point is a minimum). Combined with Parseval's theorem, $(2\pi)^2\int_{\text{all }\mathbf{x}_\perp}|\mathcal{P}_a\mathbf{E}_0|^2\,\mathrm{d}\mathbf{x}_\perp = \int_{\text{all }\mathbf{k}'}|\mathcal{F}(\mathcal{P}_a\mathbf{E}_0)|^2\,\mathrm{d}\mathbf{k}'$, this yields

$$m_0 = \frac{\int_{\text{all }\mathbf{k}'\notin\text{mask}}|\mathcal{F}(\mathcal{P}_a\mathbf{E}_0)|^2\,\mathrm{d}\mathbf{k}'}{\int_{\text{all }\mathbf{k}'}|\mathcal{F}(\mathcal{P}_a\mathbf{E}_0)|^2\,\mathrm{d}\mathbf{k}'}. \tag{A4}$$

The expression for $m_\mathbf{k}$ follows from a similar line of reasoning.

APPENDIX B: MASK RESPONSE MODEL

We compute $m_\mathbf{k}$ based on Eq. (8) for an effective Gaussian beam passing through a mask similar to the one in Fig. 3. Thus,

$$m_\mathbf{k} = \frac{\int_{\text{all }\mathbf{k}'\notin\text{mask}}\left(\mathrm{e}^{-|\mathbf{k}'-\mathbf{k}|^2W_{\text{eff}}^2/2}+\mathrm{e}^{-|\mathbf{k}'+\mathbf{k}|^2W_{\text{eff}}^2/2}\right)\mathrm{d}\mathbf{k}'}{\int_{\text{all }\mathbf{k}'}\left(\mathrm{e}^{-|\mathbf{k}'-\mathbf{k}|^2W_{\text{eff}}^2/2}+\mathrm{e}^{-|\mathbf{k}'+\mathbf{k}|^2W_{\text{eff}}^2/2}\right)\mathrm{d}\mathbf{k}'} = 1+\frac{\left(2\int_{\text{wedge}}-\int_{k'>k_{\text{mask}}}\right)\left(\mathrm{e}^{-|\mathbf{k}'-\mathbf{k}|^2W_{\text{eff}}^2/2}+\mathrm{e}^{-|\mathbf{k}'+\mathbf{k}|^2W_{\text{eff}}^2/2}\right)\mathrm{d}\mathbf{k}'}{\int_{\text{all }\mathbf{k}'}\left(\mathrm{e}^{-|\mathbf{k}'-\mathbf{k}|^2W_{\text{eff}}^2/2}+\mathrm{e}^{-|\mathbf{k}'+\mathbf{k}|^2W_{\text{eff}}^2/2}\right)\mathrm{d}\mathbf{k}'}, \tag{B1}$$

with W_{eff} being the effective Gaussian 1/e electric field beam radius in the plasma, k_{mask} being the maximum wave number covered by the central circular cutout, and "wedge" referring to an opening on one side of the mask outside the central circular cutout. The second equality in Eq. (B1) follows by noting that the integral over the central cutout, $\int_{k'<k_{\text{mask}}} = \int_{\text{all }\mathbf{k}'} - \int_{k'>k_{\text{mask}}}$, and that the integrals over the two wedges are identical. Using the standard two-dimensional Gaussian integral in the denominator and converting the remaining integrals to polar coordinates yields

$$m_\mathbf{k} = 1 + W_{\text{eff}}^2\left(\int_{k_{\text{mask}}}^{\infty} k'\,\mathrm{e}^{-(k^2+k'^2)W_{\text{eff}}^2/2}\times\left\{\frac{1}{2\pi}\int_{\theta_{\text{mask}}-\alpha(k')}^{\theta_{\text{mask}}+\alpha(k')}\left[\mathrm{e}^{kk'W_{\text{eff}}^2\cos(\theta'-\theta)}+\mathrm{e}^{-kk'W_{\text{eff}}^2\cos(\theta'-\theta)}\right]\mathrm{d}\theta' - I_0(kk'W_{\text{eff}}^2)\right\}\mathrm{d}k'\right). \tag{B2}$$

Here, $I_0(kk'W_{\text{eff}}^2) = [1/(2\pi)]\int_0^{2\pi}\mathrm{e}^{\pm kk'W_{\text{eff}}^2\cos(\theta'-\theta)}\mathrm{d}\theta'$ is the modified Bessel function of the first kind of order zero,[27] θ_{mask} is the mask angle, $\alpha(k')$ is the half-opening angle of the mask that may be a function of k', and θ is the angle of $\mathbf{k}$ (cf. Fig. 3).

We now assume that $kk'W_{\text{eff}}^2$ is large such that we can approximate I_0 by its asymptotic form,[27] $I_0(kk'W_{\text{eff}}^2) \approx \mathrm{e}^{kk'W_{\text{eff}}^2}/\sqrt{2\pi kk'W_{\text{eff}}^2}$. Since $kk'W_{\text{eff}}^2 > kk_{\text{mask}}W_{\text{eff}}^2$ in the integral and $k > k_{\text{min}}$ in order for the fluctuations to be well resolved by PCI, we can use $k_{\text{min}}k_{\text{mask}}W_{\text{eff}}^2$ as a lower bound for $kk'W_{\text{eff}}^2$ relevant to PCI. Taking $W_{\text{eff}} = 19\,\text{mm}$, which is a small value compared with those typically employed at W7-X, and setting $k_{\text{mask}} = k_{\text{min}} = 1.6\,\text{cm}^{-1}$,[3,4,6,7] we get $k_{\text{min}}k_{\text{mask}}W_{\text{eff}}^2 = 9.3$. At $k_{\text{min}}k_{\text{mask}}W_{\text{eff}}^2 = 9.3$, the asymptotic approximation for I_0 underestimates the true value by 1.4 %. This indicates that the relative error introduced by the approximation of I_0 will be less than 1.4 % in the region of $\mathbf{k}$ space well resolved by PCI at W7-X. For $[1/(2\pi)]\int_{\theta_{\text{mask}}-\alpha(k')}^{\theta_{\text{mask}}+\alpha(k')}\mathrm{e}^{kk'W_{\text{eff}}^2\cos(\theta'-\theta)}\mathrm{d}\theta'$, which is effectively an incomplete modified Bessel function of the first kind of order zero, a similar asymptotic approximation can be obtained. To do this, we note that only the region close to the maximum of the argument of the exponential ($\theta' \approx \theta$) contributes significantly to the overall value of the integral for large $kk'W_{\text{eff}}^2$. We can, thus, replace $\cos(\theta'-\theta)$ by its second-order Taylor expansion around $\theta' = \theta$, $\cos(\theta'-\theta) \approx 1-(\theta'-\theta)^2/2$, and find

$$\frac{1}{2\pi}\int_{\theta_{\text{mask}}-\alpha(k')}^{\theta_{\text{mask}}+\alpha(k')}\mathrm{e}^{kk'W_{\text{eff}}^2\cos(\theta'-\theta)}\,\mathrm{d}\theta' \approx \frac{\mathrm{e}^{kk'W_{\text{eff}}^2}}{2\pi}\int_{\theta_{\text{mask}}-\alpha(k')}^{\theta_{\text{mask}}+\alpha(k')}\mathrm{e}^{-kk'W_{\text{eff}}^2(\theta'-\theta)^2/2}\,\mathrm{d}\theta' = \frac{\mathrm{e}^{kk'W_{\text{eff}}^2}}{2\sqrt{2\pi kk'W_{\text{eff}}^2}}\left\{\mathrm{erf}\left[\frac{\sqrt{kk'}W_{\text{eff}}}{\sqrt{2}}(\theta_{\text{mask}}+\alpha(k')-\theta)\right] - \mathrm{erf}\left[\frac{\sqrt{kk'}W_{\text{eff}}}{\sqrt{2}}(\theta_{\text{mask}}-\alpha(k')-\theta)\right]\right\}, \tag{B3}$$

with erf being the error function.[27] The above approximation is similar to other asymptotic integral approximation schemes, such as Stirling's approximation for the Gamma function and the stationary phase approximation.[45] For $[1/(2\pi)]\int_{\theta_{\text{mask}}-\alpha(k')}^{\theta_{\text{mask}}+\alpha(k')}\mathrm{e}^{-kk'W_{\text{eff}}^2\cos(\theta'-\theta)}\mathrm{d}\theta'$, the same approximation is possible by noting that $\cos(\theta'-\theta) = -\cos(\theta'-\theta-\pi)$ and expanding $\cos(\theta'-\theta-\pi)$ around $\theta' = \theta+\pi$,

$$\frac{1}{2\pi}\int_{\theta_{\text{mask}}-\alpha(k')}^{\theta_{\text{mask}}+\alpha(k')}\mathrm{e}^{-kk'W_{\text{eff}}^2\cos(\theta'-\theta)}\,\mathrm{d}\theta' \approx \frac{\mathrm{e}^{kk'W_{\text{eff}}^2}}{2\sqrt{2\pi kk'W_{\text{eff}}^2}}\left\{\mathrm{erf}\left[\frac{\sqrt{kk'}W_{\text{eff}}}{\sqrt{2}}(\theta_{\text{mask}}+\alpha(k')-\theta-\pi)\right] - \mathrm{erf}\left[\frac{\sqrt{kk'}W_{\text{eff}}}{\sqrt{2}}(\theta_{\text{mask}}-\alpha(k')-\theta-\pi)\right]\right\}; \tag{B4}$$

$\theta_{\text{mask}}-\theta$ should be mapped to the region $[-\pi/2, 3\pi/2[$ for the expressions in Eqs. (B3) and (B4) to be valid. Inserting the asymptotic approximations in Eq. (B2) and completing the square in the argument of the exponential function finally yields

$$m_{\mathbf{k}} \approx 1 + \frac{W_{\mathrm{eff}}}{2\sqrt{2\pi}} \int_{k_{\mathrm{mask}}}^{\infty} \mathrm{e}^{-(k'-k)^2 W_{\mathrm{eff}}^2/2} \sqrt{\frac{k'}{k}} \times \left\{ \mathrm{erf}\left[\frac{\sqrt{kk'} W_{\mathrm{eff}}}{\sqrt{2}} (\theta_{\mathrm{mask}} + \alpha(k') - \theta) \right] - \mathrm{erf}\left[\frac{\sqrt{kk'} W_{\mathrm{eff}}}{\sqrt{2}} (\theta_{\mathrm{mask}} - \alpha(k') - \theta) \right] + \mathrm{erf}\left[\frac{\sqrt{kk'} W_{\mathrm{eff}}}{\sqrt{2}} (\theta_{\mathrm{mask}} + \alpha(k') - \theta - \pi) \right] - \mathrm{erf}\left[\frac{\sqrt{kk'} W_{\mathrm{eff}}}{\sqrt{2}} (\theta_{\mathrm{mask}} - \alpha(k') - \theta - \pi) \right] - 2 \right\} \mathrm{d}k'. \quad \text{(B5)}$$

To evaluate Eq. (B5), we employ another asymptotic approximation. This is done by noting that the integrand of Eq. (B5) contains an exponential factor, $\mathrm{e}^{-(k'-k)^2 W_{\mathrm{eff}}^2/2}$, peaking at $k' = k$ and quickly decreasing away from $k' = k$. On the other hand, the remaining part of the integrand varies slowly with respect to k' for $k \not\approx 0$. We can, therefore, in a similar to spirit to other asymptotic integral approximation schemes,[45] retain only the k' dependence of $\mathrm{e}^{-(k'-k)^2 W_{\mathrm{eff}}^2/2}$ and evaluate the remaining part of the integrand at $k' = k$. This yields

$$m_{\mathbf{k}} \approx 1 + \frac{1}{4} \mathrm{erfc}\left[\frac{(k_{\mathrm{mask}} - k) W_{\mathrm{eff}}}{\sqrt{2}} \right] \times \left\{ \mathrm{erf}\left[\frac{k W_{\mathrm{eff}}}{\sqrt{2}} (\theta_{\mathrm{mask}} + \alpha(k) - \theta) \right] - \mathrm{erf}\left[\frac{k W_{\mathrm{eff}}}{\sqrt{2}} (\theta_{\mathrm{mask}} - \alpha(k) - \theta) \right] + \mathrm{erf}\left[\frac{k W_{\mathrm{eff}}}{\sqrt{2}} (\theta_{\mathrm{mask}} + \alpha(k) - \theta - \pi) \right] - \mathrm{erf}\left[\frac{k W_{\mathrm{eff}}}{\sqrt{2}} (\theta_{\mathrm{mask}} - \alpha(k) - \theta - \pi) \right] - 2 \right\}, \quad \text{(B6)}$$

where erfc is the complementary error function.[27] For $k < k_{\mathrm{mask}}$, we set $\alpha(k) = \alpha(k_{\mathrm{mask}}^+)$ to avoid discontinuities, but note that Eq. (B6) cannot be expected to provide accurate results for $k < k_{\mathrm{mask}}$ due to the limitations of the simplified mask model.

APPENDIX C: RESPONSE OF A STRAIGHT MASK

As straight masks have been, and are currently, employed in a number of different PCI systems,[5,15,16,18] we compute m_0 and $m_{\mathbf{k}}$ for a Gaussian beam in the plasma with such masks, to facilitate the use of the theory developed here at other devices. As illustrated in Fig. 17, $m_{\mathbf{k}}$ for a straight mask can be obtained using Eq. (B6) with $\alpha(k) = \arcsin(k_{\mathrm{mask}}/k)$ (for $k > k_{\mathrm{mask}}$) or $\arcsin(1) = \pi/2$ (for $k < k_{\mathrm{mask}}$); k_{mask} is the half-width of the mask slit in $\mathbf{k}'$ space (cf. Fig. 17). This is in agreement with previous estimates.[5,18]

To compute m_0 for a straight mask, we note that the result will be independent of θ_{mask} due to the θ' symmetry of $\mathcal{F}(\mathcal{P}_a \mathbf{E}_0)$ from

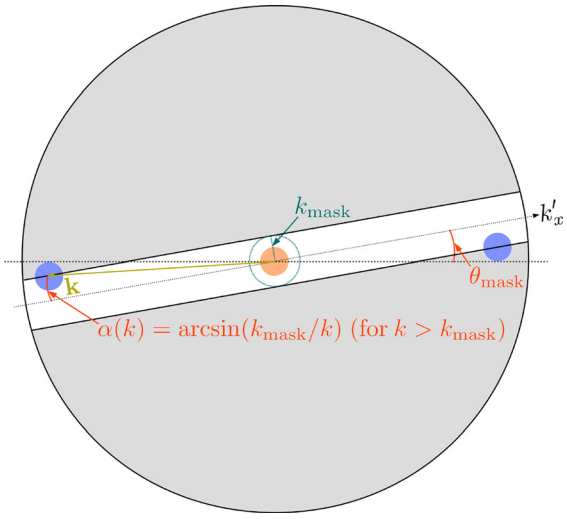

FIG. 17. Illustration of a straight mask in $\mathbf{k}'$ space. When calculating m_0, the k'_x axis is oriented parallel to the groove of the straight mask.

Eq. (16). We can, therefore, orient the k'_x axis along the mask groove, as shown in Fig. 17, such that the integration limits in the numerator of Eq. (7) are $k'_x \in]-\infty, \infty[$ and $k'_y \in]-k_{\mathrm{mask}}, k_{\mathrm{mask}}[$. Performing the integral over the circular aperture near the plasma in Cartesian coordinates, combined with the definitions of $\mathcal{F}$ and $\mathcal{F}^*$, then yields

$$|\mathcal{F}(\mathcal{P}_a \mathbf{E}_0)|^2 = |\mathbf{E}_0(0)|^2 \left[\int_{-a}^{a} \left(\int_{-\sqrt{a^2-x'^2}}^{\sqrt{a^2-x'^2}} \mathrm{e}^{-(x'^2+y'^2)/W^2 - \mathrm{i}(k'_x x' + k'_y y')} \mathrm{d}y' \right) \mathrm{d}x' \right] \times \left[\int_{-a}^{a} \left(\int_{-\sqrt{a^2-x''^2}}^{\sqrt{a^2-x''^2}} \mathrm{e}^{-(x''^2+y''^2)/W^2 + \mathrm{i}(k'_x x'' + k'_y y'')} \mathrm{d}y'' \right) \mathrm{d}x'' \right]. \quad \text{(C1)}$$

Equation (C1) can be plugged into Eq. (7), allowing the k'_x and k'_y integrals to be evaluated, $\int_{-\infty}^{\infty} \mathrm{e}^{\mathrm{i}k'_x(x''-x')} \mathrm{d}k'_x = 2\pi\delta(x''-x')$ (where δ is the Dirac delta distribution) and $\int_{-k_{\mathrm{mask}}}^{k_{\mathrm{mask}}} \mathrm{e}^{\mathrm{i}k'_y(y''-y')} \mathrm{d}k'_y = 2\sin[k_s(y''-y')]/(y''-y')$, with the result that

$$m_0 = \frac{4}{\pi^2 (1 - \mathrm{e}^{-2a^2/W^2}) W^2} \times \int_0^a \left(\int_{-\sqrt{a^2-x'^2}}^{\sqrt{a^2-x'^2}} \left\{ \int_{-\sqrt{a^2-x'^2}}^{\sqrt{a^2-x'^2}} \frac{\sin[k_{\mathrm{mask}}(y''-y')]}{y''-y'} \times \mathrm{e}^{-(2x'^2+y'^2+y''^2)/W^2} \mathrm{d}y'' \right\} \mathrm{d}y' \right) \mathrm{d}x'; \quad \text{(C2)}$$

in Eq. (C2), we have also used the fact that the integrand is an even function of x', along with Eq. (17). While, in general, the integrals in Eq. (C2) cannot be evaluated analytically, they involve a well-behaved integrand and a finite integration domain. This makes Eq. (C2) suitable for numerical evaluation, which is further facilitated by rewriting it as

$$m_0 = \frac{\sqrt{8}k_{\rm mask}W}{\pi^2(1-e^{-2a^2/W^2})} \times \int_0^{\sqrt{2}a/W}\left(\int_{-\sqrt{a^2/W^2-\xi^2/2}}^{\sqrt{a^2/W^2-\xi^2/2}}\left\{\int_{-\sqrt{a^2/W^2-\xi^2/2}}^{\sqrt{a^2/W^2-\xi^2/2}}\mathrm{sinc}\left[\frac{k_{\rm mask}W(\eta'-\eta)}{\pi}\right] \times e^{-\xi^2-\eta^2-\eta'^2}d\eta'\right\}d\eta\right)d\xi, \quad \text{(C3)}$$

where $\mathrm{sinc}(\cdot) = \sin(\pi\cdot)/(\pi\cdot)$. Equation (C3) is evaluated using the SciPy function `tplquad`.

Before computing m_0 numerically, we determine its value analytically in the Gaussian and Airy disk limits. For $a \to \infty$, $e^{-2a^2/W^2} \to 0$ and the limits of integration in Eq. (C2) can be extended to $\pm\infty$. Thus, the y' and y'' integrals can be evaluated using the convolution theorem,[45] while the x' integral is a standard Gaussian integral, giving

$$m_0(\text{Gaussian}) = \mathrm{erf}\left(\frac{k_{\rm mask}W}{\sqrt{2}}\right). \quad \text{(C4)}$$

This is also the result for a pure Gaussian beam. For $W \to \infty$, $1 - e^{-2a^2/W^2} \to 2a^2/W^2$ and the Gaussian functions in the integrand of Eq. (C2) may be set to 1, yielding

$$m_0(\text{Airy Disk}) = \frac{16}{3\pi^2}\,k_{\rm mask}a\,{}_2F_3\left(1/2, 1; 3/2, 3/2, 5/2; -k_{\rm mask}^2a^2\right), \quad \text{(C5)}$$

where ${}_2F_3$ is the generalized hypergeometric series;[28] this is also the Airy disk result.

We now plot m_0 computed based on Eq. (C3), along with the asymptotic versions from Eqs. (C4) and (C5), vs W/a in Fig. 18. Figure 18 appears qualitatively similar to Fig. 4, with the exact m_0 following the Gaussian approximation for small W/a, but eventually reaching a maximum and decreasing toward the Airy disk value for large W/a. The value of $k_{\rm mask} = 2.205/a$ (corresponding to a slit width of 0.96 mm at W7-X) in Fig. 18 has been chosen such that the estimated W at the maximum of m_0, $\sqrt{2a/k_{\rm mask}} = 0.9524a$, corresponds to the typical value of $W = 40$ mm at W7-X. This is confirmed by numerical evaluation of the position of the maximum of m_0 in Fig. 18.

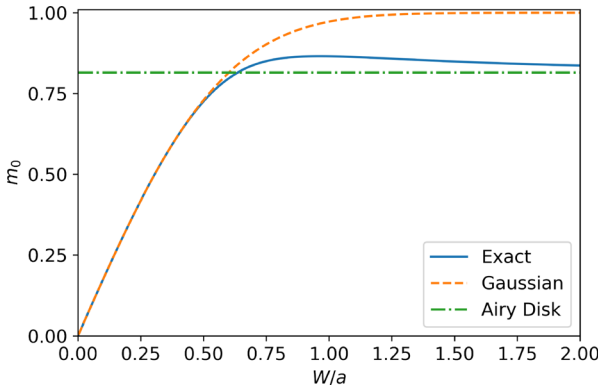

FIG. 18. m_0 vs W/a using the exact (solid line), Gaussian (dashed line), and Airy disk (dashed-dotted line) models for a straight mask with $k_{\rm mask}a = 2.205$. The value of $k_{\rm mask}a$ is chosen such that the estimated maximum of m_0 occurs at $W = \sqrt{2a/k_{\rm mask}} = 40$ mm for W7-X-like parameters.

APPENDIX D: FIT QUALITY OF EFFECTIVE GAUSSIAN MODEL

The fit quality of $\mathcal{M}_{\mathbf{k}} = m_0 m_{\mathbf{k}}$ resulting from Eqs. (19) and (22), with $W_{\rm eff}$ from Eq. (24), is illustrated in Fig. 19 for $k = 3.7\,\mathrm{cm}^{-1}$ (the typical sound wave calibration k at W7-X[4]), $a = 42$ mm, $\alpha = 5°$, and $k_{\rm mask} = 1.6\,\mathrm{cm}^{-1}$. In the top, middle, and bottom panels of Fig. 19, $W = 20$, 40, and 400 mm, respectively. Apart from the approximate $\mathcal{M}_{\mathbf{k}}$, we also plot $\mathcal{M}_{\mathbf{k}}$ calculated by numerical evaluation of the $m_{\mathbf{k}}$

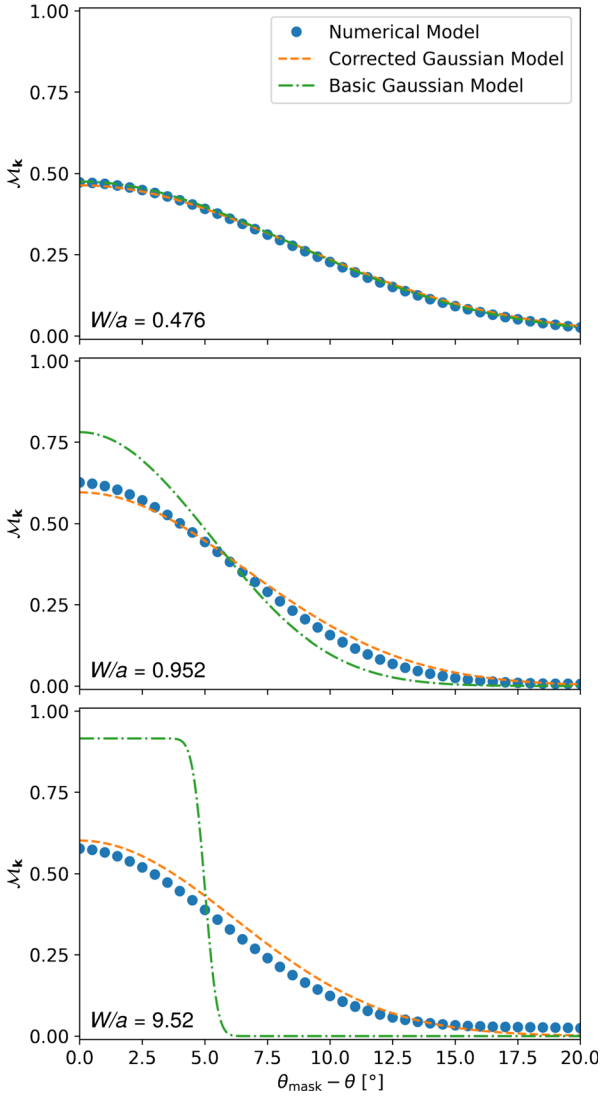

FIG. 19. $\mathcal{M}_{\mathbf{k}}$ calculated numerically (solid circles) and using Eq. (22) with $W_{\rm eff}$ from Eq. (24) (dashed lines) or $W_{\rm eff} = W$ (dashed-dotted lines) for $\alpha = 5°$, $k = 3.7\,\mathrm{cm}^{-1}$, $a = 42$ mm, and $k_{\rm mask} = 1.6\,\mathrm{cm}^{-1}$. In the top, middle, and bottom panels, $W = 20$, 40, and 400 mm, respectively.

given by Eq. (8), with $\mathbf{E}_0$ from Eq. (15), and $\mathcal{M}_\mathbf{k}$ calculated using the $m_\mathbf{k}$ from Eq. (22) with $W_{\text{eff}} = W$. For $W = 20$ mm, corresponding to $W/a = 0.476$, all three models are in close agreement, showing that the approximate Gaussian $m_\mathbf{k}$ from Eq. (22) closely reproduces the numerical result when the influence of the aperture is small ($W/a < 0.5$, cf. Fig. 5). When $W = 40$ mm, which is the typical case at W7-X and corresponds to $W/a = 0.952$, the approximate $\mathcal{M}_\mathbf{k}$ with W_{eff} from Eq. (24) remains close to the numerical result, while the approximate form with $W_{\text{eff}} = W$ has a significantly narrower transition region around $\theta_{\text{mask}} - \theta = \alpha$. This indicates that the influence of the aperture on the beam spot size can be modeled accurately by the W_{eff} from Eq. (24) at typical W7-X parameters. For $W = 400$ mm, corresponding to $W/a = 9.52$ and used to investigate a case close to the Airy disk diffraction pattern, the approximate $\mathcal{M}_\mathbf{k}$ with W_{eff} from Eq. (24) still resembles the numerical result. It does, however, fall off significantly faster for large $\theta_{\text{mask}} - \theta$, due to the use of a Gaussian function to approximate the Airy disk diffraction pattern. On the other hand, the approximate $\mathcal{M}_\mathbf{k}$ with $W_{\text{eff}} = W$ shows an almost step-like behavior around $\theta_{\text{mask}} - \theta = \alpha$, indicating that the ability of the mask to provide localized PCI measurements is almost entirely limited by diffraction from the aperture in this case. Based on Fig. 19, we conclude that the approximate $\mathcal{M}_\mathbf{k}$ with W_{eff} from Eq. (24) is close to the numerical value for the k and W values relevant to W7-X.

APPENDIX E: COMPUTATION OF THE FULL SYNTHETIC PCI SIGNAL WITH A MASK

To evaluate Eq. (2) numerically, $\mathcal{F}$ and $\mathcal{F}^{-1}$ are computed using the `fft.fft2` and `fft.ifft2` functions from NumPy, respectively. $\mathbf{E}_a$ from Eq. (1) is evaluated on a 256×256 point (x, y) grid with linear spacing in the intervals $x, y \in [-a, a]$. $\mathcal{F}(\mathbf{E}_a)$ is evaluated on a 4096×4096 point (k'_x, k'_y) grid (to ensure convergence) with linear spacing in the intervals $k'_x, k'_y \in [-k'_{\text{max}}, k'_{\text{max}}]$, where $k'_{\text{max}} = 255\pi/(2a) = 95.4\,\text{cm}^{-1}$ is the Nyquist wave number of the (x, y) grid. The larger number of points in the (k'_x, k'_y) grid is obtained by zero-padding of $\mathbf{E}_a$. Next, T_p and $\mathcal{P}_m$ are evaluated on the (k'_x, k'_y) grid, and $\mathcal{F}^{-1}[T_p \mathcal{P}_m \mathcal{F}(\mathbf{E}_a)]$ is computed on an (x, y) grid similar to the one used for $\mathbf{E}_a$ by removing the zero-padding. We then obtain I_{im}, which can be numerically integrated over the scaled PCI detector elements, as described in Ref. 7. The power on each detector element is finally split into a DC part and an AC part, used to calculate the noise and PCI signal, respectively.[7]

APPENDIX F: MHD MODE MODEL FOR SYNTHETIC PCI INVESTIGATIONS

We use an *ad hoc* MHD mode model that is conceptually similar to the simplified model used for turbulence studies in Ref. 6. The MHD mode is modeled by modifying $|\rho_{\text{tor}}|$ to

$$\rho_{\text{arg}} = |\rho_{\text{tor}}| + \tilde{\rho}_{\text{tor}} \sin(m\theta^* - 2\pi f_{\text{MHD}} t + \theta_0^*), \tag{F1}$$

where m is the poloidal mode number, θ^* is the poloidal PEST angle,[46] $\tilde{\rho}_{\text{tor}} = \tilde{\rho}_{\text{tor}}(|\rho_{\text{tor}}|)$ is the radial amplitude profile of the MHD mode, f_{MHD} is the rotation frequency of the MHD mode, and θ_0^* is the phase of the MHD mode at $\theta^*, t = 0$. While Eq. (F1) describes a simple MHD mode containing only one m component, it can easily be generalized to include modes with ballooning character through the introduction of a θ^*-dependent $\tilde{\rho}_{\text{tor}}$. We do, however, note that localization techniques relying on the mode structure being aligned with the background $\mathbf{B}$ will not necessarily be valid for ballooning modes.[47] Following Ref. 41, we consider a Gaussian $\tilde{\rho}_{\text{tor}}$,

$$\tilde{\rho}_{\text{tor}} = a_0\, \mathrm{e}^{-(|\rho_{\text{tor}}| - \rho_0)^2/w^2}, \tag{F2}$$

with ρ_0 being the radial center of the mode, w being the radial width of the mode, and a_0 being the amplitude of the mode at its center. Assuming that the background electron density, $n_{e0} = n_{e0}(|\rho_{\text{tor}}|)$, remains constant on the perturbed flux surfaces, we can then obtain $\tilde{n}_e = n_{e0}(\rho_{\text{arg}}) - n_{e0}(|\rho_{\text{tor}}|)$, which is used as input for the synthetic PCI diagnostic.[7] For the MHD mode shown in Fig. 16, we have used the n_{e0} profile from Fig. 2 of Ref. 33. The synthetic PCI spectra in Fig. 15 are computed by adding the turbulent $\tilde{n}_e$ used for computing Fig. 13 to the $\tilde{n}_e$ associated with the MHD mode.

REFERENCES

[1] C. D. Beidler, H. M. Smith, A. Alonso, T. Andreeva, J. Baldzuhn, M. N. A. Beurskens, M. Borchardt, S. A. Bozhenkov, K. J. Brunner, H. Damm, M. Drevlak, O. P. Ford, G. Fuchert, J. Geiger, P. Helander, U. Hergenhahn, M. Hirsch, U. Höfel, Y. O. Kazakov, R. Kleiber, M. Krychowiak, S. Kwak, A. Langenberg, H. P. Laqua, U. Neuner, N. A. Pablant, E. Pasch, A. Pavone, T. S. Pedersen, K. Rahbarnia, J. Schilling, E. R. Scott, T. Stange, J. Svensson, H. Thomsen, Y. Turkin, F. Warmer, R. C. Wolf, D. Zhang, and the W7-X Team. "Demonstration of reduced neoclassical energy transport in Wendelstein 7-X," Nature **596**, 221–226 (2021).

[2] T. Sunn Pedersen, I. Abramovic, P. Agostinetti, M. Agredano Torres, S. Äkäslompolo, J. Alcuson Belloso, P. Aleynikov, K. Aleynikova, M. Alhashimi, A. Ali *et al.*, "Experimental confirmation of efficient island divertor operation and successful neoclassical transport optimization in Wendelstein 7-X," Nucl. Fusion **62**, 042022 (2022).

[3] E. M. Edlund, M. Porkolab, Z. Huang, O. Grulke, L.-G. Böttger, C. von Sehren, and A. von Stechow, "Overview of the Wendelstein 7-X phase contrast imaging diagnostic," Rev. Sci. Instrum. **89**, 10E105 (2018).

[4] Z. Huang, E. Edlund, M. Porkolab, J.-P. Bähner, L.-G. Böttger, C. von Sehren, A. von Stechow, and O. Grulke, "The Wendelstein 7-X phase contrast imaging diagnostic," J. Instrum. **16**, P01014 (2021).

[5] S. Kado, T. Irie, K. Muraoka, K. Matsuo, K. Tanaka, K. Kondo, F. Sano, and T. Obiki, "Improvement of the laser phase contrast imaging method for measuring the spatial distribution of electron density fluctuations in Heliotron E," Jpn. J. Appl. Phys., Part 1 **34**, 6492–6500 (1995).

[6] J.-P. Bähner, J. A. Alcusón, S. K. Hansen, A. von Stechow, O. Grulke, T. Windisch, H. M. Smith, Z. Huang, E. Edlund, M. Porkolab, M. N. A. Beurskens, S. A. Bozhenkov, O. P. Ford, N. Pablant, G. G. Plunk, A. Bañón Navarro, F. Jenko, and The W7-X Team, "Phase contrast imaging measurements and numerical simulations of turbulent density fluctuations in gas-fueled ECRH discharges in Wendelstein 7-X," J. Plasma Phys. **87**, 905870314 (2021).

[7] S. K. Hansen, M. Porkolab, J.-P. Bähner, Z. Huang, A. von Stechow, O. Grulke, E. M. Edlund, F. Wilms, A. Bañón Navarro, F. Jenko, and E. Sánchez, "Development of a synthetic phase contrast imaging for turbulence studies at Wendelstein 7-X," Plasma Phys. Controlled Fusion **64**, 095011 (2022).

[8] T. Estrada, D. Carralero, T. Windisch, E. Sánchez, J. M. García-Regaña, J. Martínez-Fernández, A. de la Peña, J. L. Velasco, J. A. Alonso, M. Beurskens, S. Bozhenkov, H. Damm, G. Fuchert, R. Kleiber, N. Pablant, E. Pasch, and the W7-X Team, "Radial electric field and density fluctuations measured by Doppler reflectometry during the post-pellet enhanced confinement phase in W7-X," Nucl. Fusion **61**, 046008 (2021).

[9]H. Trimino Mora, T. P. Crowley, D. R. Demers, P. J. Fimognari, O. Grulke, and R. Laube, "Conceptual design of a heavy ion beam probe diagnostic for the Wendelstein 7-X stellarator," Rev. Sci. Instrum. **93**, 113309 (2022).
[10]J.-P. Bähner, L. Podavini, M. Porkolab, A. von Stechow, S. K. Hansen, E. M. Edlund, S. A. Bozhenkov, A. Zocco, O. Grulke, and the Wendelstein 7-X Team, "Magnetic configuration dependence of turbulent core density fluctuations in Wendelstein 7-X," Europhys. Conf. Abstracts **47A**, P2.077 (2023), https://lac913.epfl.ch/epsppd3/2023/html/Tu/Tu_MCF77_Bahner.pdf.
[11]C. Slaby, S. Äkäslompolo, M. Borchardt, J. Geiger, R. Kleiber, A. Könies, S. Bozhenkov, C. Brandt, A. Dinklage, M. Dreval, O. Ford, G. Fuchert, D. Hartmann, M. Hirsch, U. Höfel, Z. Huang, P. McNeely, N. Pablant, K. Rahbarnia, N. Rust, J. Schilling, A. von Stechow, H. Thomsen, and the Wendelstein 7-X Team, "Investigation of mode activity in NBI-heated experiments of Wendelstein 7-X," Nucl. Fusion **60**, 112004 (2020).
[12]K. Rahbarnia, S. Vaz Mendes, C. Büschel, C. Brandt, H. Thomsen, A. von Stechow, J.-P. Bähner, S. K. Hansen, R. Kleiber, C. Slaby, A. Könies, and Wendelstein 7-X Team, "Alfvén eigenmode dynamics during the recent operational phase at the Wendelstein 7-X stellarator," Europhys. Conf. Abstracts **47A**, P2.074 (2023), https://lac913.epfl.ch/epsppd3/2023/html/Tu/Tu_MCF74_Rahbarnia.pdf.
[13]L. Lin, M. Porkolab, E. M. Edlund, J. C. Rost, C. L. Fiore, M. Greenwald, Y. Lin, D. R. Mikkelsen, N. Tsujii, and S. J. Wukitch, "Studies of turbulence and transport in Alcator C-Mod H-mode plasmas with phase contrast imaging and comparisons with GYRO," Phys. Plasmas **16**, 012502 (2009).
[14]J. C. Rost, L. Lin, and M. Porkolab, "Development of a synthetic phase contrast imaging diagnostic," Phys. Plasmas **17**, 062506 (2010).
[15]A. Iantchenko, S. Coda, S. Brunner, G. Merlo, J. Ball, and F. Margairaz, "A synthetic phase-contrast imaging diagnostic with spatial filtering for gyrokinetic simulations," Plasma Phys. Controlled Fusion **65**, 025005 (2023).
[16]L. Lin, E. M. Edlund, M. Porkolab, Y. Lin, and S. J. Wukitch, "Vertical localization of phase contrast imaging diagnostic in Alcator C-Mod," Rev. Sci. Instrum. **77**, 10E918 (2006).
[17]K. Tanaka, C. A. Michael, L. N. Vyacheslavov, A. L. Sanin, K. Kawahata, T. Akiyama, T. Tokuzawa, and S. Okajima, "Two-dimensional phase contrast imaging for local turbulence measurements in large helical device (invited)," Rev. Sci. Instrum. **79**, 10E702 (2008).
[18]J. R. Dorris, J. C. Rost, and M. Porkolab, "Localized measurement of short wavelength plasma fluctuations with the DIII-D phase contrast imaging diagnostic," Rev. Sci. Instrum. **80**, 023503 (2009).
[19]C. A. Michael, K. Tanaka, L. Vyacheslavov, A. Sanin, and K. Kawahata, "Two-dimensional wave-number spectral analysis techniques for phase contrast imaging turbulence imaging data on large helical device," Rev. Sci. Instrum. **86**, 093503 (2015).
[20]S. K. Hansen, M. Porkolab, J.-P. Bähner, A. von Stechow, O. Grulke, E. M. Edlund, and the Wendelstein 7-X Team, "Localized phase contrast imaging measurements at Wendelstein 7-X," Europhys. Conf. Abstracts **47A**, P5.018 (2023), https://lac913.epfl.ch/epsppd3/2023/html/Fr/Fr_MCF18_Hansen.pdf.
[21]A. v. Stechow, O. Grulke, Th. Wegner, J. H. E. Proll, J. A. Alcusón, H. M. Smith, J. Baldzuhn, C. D. Beidler, M. N. A. Beurskens, S. A. Bozhenkov, E. Edlund, B. Geiger, Z. Huang, O. P. Ford, G. Fuchert, A. Langenberg, N. Pablant, E. Pasch, M. Porkolab, K. Rahbarnia, J. Schilling, E. R. Scott, H. Thomsen, L. Vanó, G. Weir, and The W7-X Team, "Suppression of core turbulence by profile shaping in Wendelstein 7-X," arXiv:2010.02160 (2020).
[22]H. Sakai, K. Tanaka, and T. Kinoshita, "Development of sweeping detector phase contrast imaging in large helical device," J. Instrum. **18**, C12019 (2023).
[23]A. Truc, A. Quéméneur, P. Hennequin, D. Grésillon, F. Gervais, C. Laviron, J. Olivain, S. K. Saha, and P. Devynck, "ALTAIR: An infrared laser scattering diagnostic on the TORE SUPRA tokamak," Rev. Sci. Instrum. **63**, 3716–3724 (1992).
[24]O. Grulke, C. Albert, J. A. Alcuson Belloso, P. Aleynikov, K. Aleynikova, A. Alonso, G. Anda, T. Andreeva, M. Arvanitou, E. Ascasibar *et al.*, "Overview of the first Wendelstein 7-X long pulse campaign with fully water-cooled plasma facing components," Nucl. Fusion (submitted) (2024).
[25]S. Coda, "An experimental study of turbulence by phase-contrast imaging in the DIII-D tokamak," Ph.D. thesis (Massachusetts Institute of Technology, Cambridge, 1997).
[26]M. Born and E. Wolf, *Principles of Optics*, 7th (expanded) ed. (Cambridge University Press, Cambridge, 2002).
[27]M. Abramowitz and I. A. Stegun, *Handbook of Mathematical Functions* (National Bureau of Standards, Washington, DC, 1964), 10th printing.
[28]I. S. Gradshteyn and I. M. Ryzhik, *Table of Integrals, Series, and Products*, 7th ed. (Elsevier Academic Press, Amsterdam, 2007).
[29]G. B. Airy, "On the diffraction of an object-glass with circular aperture," Trans. Cambridge Philos. **5**, 283–291 (1835), https://archive.org/details/transactionsofca05camb/page/n305/mode/2up.
[30]B. Zhang, J. Zerubia, and J.-C. Olivo-Marin, "Gaussian approximations of fluorescence microscope point-spread function models," Appl. Opt. **46**, 1819–1829 (2007).
[31]T. Andreeva, J. Geiger, A. Dinklage, G. Wurden, H. Thomsen, K. Rahbarnia, J. C. Schmitt, M. Hirsch, G. Fuchert, C. Nührenberg, A. Alonso, C. D. Beidler, M. N. A. Beurskens, S. Bozhenkov, R. Brakel, C. Brandt, V. Bykov, M. Grahl, O. Grulke, C. Killer, G. Kocsis, T. Klinger, A. Krämer-Flecken, S. Lazerson, M. Otte, N. Pablant, J. Schilling, T. Windisch, and the W7-X Team, "Magnetic configuration scans during divertor operation of Wendelstein 7-X," Nucl. Fusion **62**, 026032 (2022).
[32]S. P. Hirshman, W. I. van Rij, and P. Merkel, "Three-dimensional free boundary calculations using a spectral Green's function method," Comput. Phys. Commun. **43**, 143–155 (1986).
[33]A. Bañón Navarro, G. Merlo, G. G. Plunk, P. Xanthopoulos, A. von Stechow, A. Di Siena, M. Maurer, F. Hindenlang, F. Wilms, and F. Jenko, "Global gyrokinetic simulations of ITG turbulence in the magnetic configuration space of the Wendelstein 7-X stellarator," Plasma Phys. Controlled Fusion **62**, 105005 (2020).
[34]E. M. Edlund, M. Porkolab, G. J. Kramer, L. Lin, Y. Lin, and S. J. Wukitch, "Observation of reversed shear Alfvén eigenmodes between sawtooth crashes in the Alcator C-Mod tokamak," Phys. Rev. Lett. **102**, 165003 (2009).
[35]E. M. Edlund, M. Porkolab, G. J. Kramer, L. Lin, Y. Lin, and S. J. Wukitch, "Phase contrast imaging measurements of reversed shear Alfvén eigenmodes during sawteeth in Alcator C-Mod," Phys. Plasmas **16**, 056106 (2009).
[36]E. M. Edlund, M. Porkolab, G. J. Kramer, L. Lin, Y. Lin, N. Tsujii, and S. J. Wukitch, "Experimental study of reversed shear Alfvén eigenmodes during the current ramp in the Alcator C-Mod tokamak," Plasma Phys. Controlled Fusion **52**, 115003 (2010).
[37]K. Rahbarnia, H. Thomsen, J. Schilling, S. vaz Mendes, M. Endler, R. Kleiber, A. Könies, M. Borchardt, C. Slaby, T. Bluhm, M. Zilker, B. B. Carvalho, and Wendelstein 7-X Team, "Alfvénic fluctuations measured by in-vessel Mirnov coils at the Wendelstein 7-X stellarator," Plasma Phys. Controlled Fusion **63**, 015005 (2021).
[38]S. Vaz Mendes, K. Rahbarnia, C. Slaby, H. Thomsen, J. Schilling, M. Borchardt, R. Kleiber, A. Könies, J.-P. Bähner, A. von Stechow, T. Sunn Pedersen, T. Klinger, and the W7-X Team, "Broadband Alfvénic excitation correlated to turbulence level in the Wendelstein 7-X stellarator plasmas," Nucl. Fusion **63**, 096008 (2023).
[39]C. Büschel, R. Kleiber, A. Könies, M. Drevlak, M. Borchardt, K. Rahbarnia, H. Thomsen, S. Vaz Mendes, C. Brandt, J. Knauer, K. J. Brunner, and Wendelstein 7-X Team, "Synthetic Mirnov diagnostic for the validation of experimental observations," Rev. Sci. Instrum. **95**, 023506 (2024).
[40]C. Brandt, J. Schilling, H. Thomsen, T. Broszat, R. Laube, T. Schröder, T. Andreeva, M. N. A. Beurskens, S. A. Bozhenkov, K. J. Brunner, A. Card, C. Cordes, H. Damm, G. Fuchert, K. Gallowski, R. Gutzmann, J. Knauer, H. P. Laqua, M. Marquardt, P. Nelde, U. Neuner, E. Pasch, K. Rahbarnia, J. Recknagel, M. Schülke, E. R. Scott, T. Sieber, and the W7-X Team, "Soft x-ray tomography measurements in the Wendelstein 7-X stellarator," Plasma Phys. Controlled Fusion **62**, 035010 (2020).
[41]M. B. Dreval, C. Brandt, J. Schilling, H. Thomsen, A. Beletskii, A. Könies, and the W7-X Team, "Determination of poloidal mode numbers of MHD modes and their radial location using a soft x-ray camera array in the Wendelstein 7-X stellarator," Plasma Phys. Controlled Fusion **63**, 065006 (2021).
[42]M. Dreval, C. Xiao, S. Elgriw, D. Trembach, S. Wolfe, and A. Hirose, "Determination of radial location of rotating magnetic islands by use of poloidal soft x-ray detector arrays in the STOR-M tokamak," Rev. Sci. Instrum. **82**, 053503 (2011).

[43]M. B. Dreval, A. M. Shapoval, F. I. Ozherelyev, and M. M. Makhov, "Design of multichord h_α detector arrays for the U-3M torsatron and identification of rotating plasma perturbations," Rev. Sci. Instrum. **87**, 073503 (2016).
[44]A. von Stechow, S. G. Baek, J.-P. Bähner, S. Ballinger, D. Cipciar, E. Edlund, O. Grulke, S. K. Hansen, C. Killer, S. Kwak, M. Krychowiak, A. Pavone, M. Porkolab, J. Svensson, J. L. Terry, and the W7-X Team, "Characterizing core and edge turbulence regimes with fluctuation imaging diagnostics in Wendelstein 7-X," Nucl. Fusion (submitted) (2024).
[45]G. B. Arfken and H. J. Weber, *Mathematical Methods for Physicists*, 6th ed. (Elsevier Academic Press, Amsterdam, 2005).
[46]R. C. Grimm, J. M. Greene, and J. L. Johnson, "Computation of the magnetohydrodynamic spectrum in axisymmetric toroidal confinement systems," in *Controlled Fusion*, Methods in Computational Physics: Advances in Research and Applications Vol. 16, edited by J. Killeen (Elsevier, Amsterdam, 1976), p. 253.
[47]H. Zohm, *Magnetohydrodynamic Stability of Tokamaks* (Wiley-VCH, Weinheim, 2015).